

Unmixing Optical Signals from Undersampled Volumetric Measurements by Filtering the Pixel Latent Variables

Catherine Bouchard^{1,2}, Andréanne Deschênes^{1,2},
Vincent Boulanger^{3,6}, Jean-Michel Bellavance¹, Julia Chabbert¹,
Alexy Pelletier-Rioux¹, Flavie Lavoie-Cardinal^{1,2,4*},
Christian Gagné^{2,5,7*}

¹CERVO Brain Research Centre, Université Laval, Québec, QC, Canada.

²Institute Intelligence and Data, Université Laval, Québec, QC, Canada.

³Centre for Optics, Photonics and Lasers, Université Laval, Québec, QC, Canada.

⁴Dep. of Psychiatry and Neuroscience, FMed, Université Laval, Québec, QC, Canada.

⁵Dep. of Electrical Eng. and Computer Eng., FSG, Université Laval, Québec, QC, Canada.

⁶Dep. of Physics, Physics Eng. and Optics, FSG, Université Laval, Québec, QC, Canada.

⁷Canada-CIFAR AI Chair.

*Corresponding author(s). E-mail(s):

flavie.lavoie-cardinal@cervo.ulaval.ca; christian.gagne@gel.ulaval.ca;

Contributing authors: catherine.bouchard.22@ulaval.ca;

andreanne.deschenes.1@ulaval.ca; vincent.boulanger.3@ulaval.ca;

jean-michel.bellavance.1@ulaval.ca; julia.chabbert.1@ulaval.ca;

alexypelletier-rioux.1@ulaval.ca;

Abstract

The development of signal unmixing algorithms is essential for leveraging multimodal datasets acquired through a wide array of scientific imaging technologies, including hyperspectral or time-resolved acquisitions. In experimental physics, enhancing the spatio-temporal resolution or expanding the number of detection channels often leads to diminished sampling rate and signal-to-noise ratio (SNR), significantly affecting the efficacy of signal unmixing algorithms. We propose *Latent Unmixing*, a new approach which applies band-pass filters to the latent space of a multi-dimensional convolutional neural network to disentangle overlapping signal components. It enables better isolation and quantification of individual signal contributions, especially in the context of undersampled distributions. Using multi-dimensional convolution kernels to process all dimensions simultaneously enhances the network's ability to extract information from adjacent pixels, and time- or spectral-bins. This approach enables more effective separation of components in cases where individual pixels do not provide clear, well-resolved information. We showcase the method's practical use in experimental physics through two test cases that highlight the versatility of our approach: fluorescence lifetime microscopy and mode decomposition in optical fibers. The latent unmixing method extracts valuable information from complex signals that cannot be resolved by standard methods. It opens new possibilities in optics and photonics for multichannel separations at an increased sampling rate.

Keywords: channel unmixing, latent space, 3D U-Net, fluorescence lifetime microscopy, S² imaging, signal separation

1 Introduction

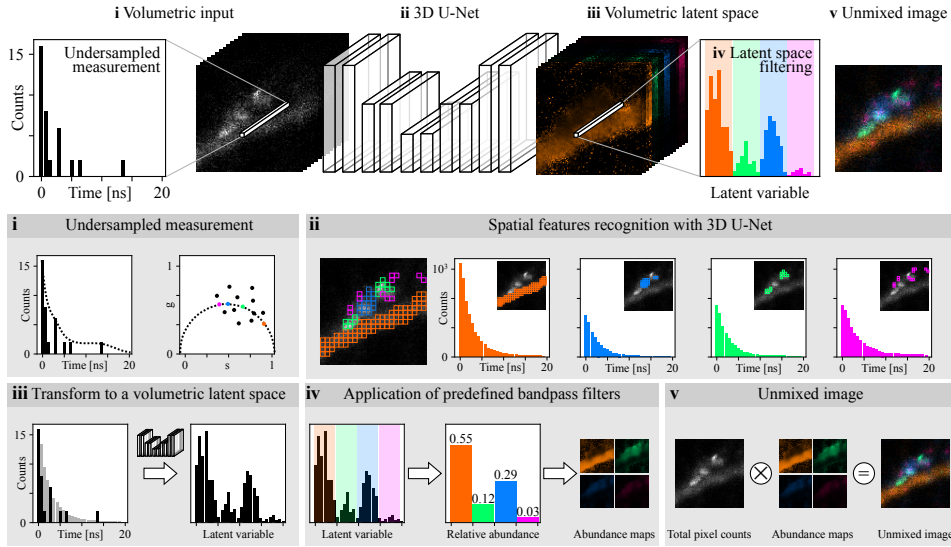


Fig. 1 The *Latent Unmixing* method maps volumetric undersampled measurements (i) using a 3D U-Net (ii) to a latent space (iii) where pre-defined bandpass filters (iv) are applied to retrieve the relative abundance of each contributing component (v). i, Methods relying on well-defined distributions (left; curve-fitting, right; phasor analysis) cannot retrieve the relative abundance of multiple components from undersampled distributions. ii, The 3D U-Net is trained to recognize spatial features indicative of distinctive structures. The resulting representation combines the information from the pixel ensemble corresponding to continuous structures in the image, instead of the pixel-wise undersampled input. iii, The information decoded from the spatial features is exploited to project the distribution of each pixel to the latent space. iv, Pre-defined filters are applied to the latent representation to extract the abundance of each component. v, The measured counts are multiplied with the abundance maps, resulting in the predicted unmixed image.

Signal unmixing refers to the technique of breaking down a measurement into its unique constituents and their respective proportions. This concept is often associated with spectral signal analysis, where the challenge lies in accurately identifying the abundance of different components from their overlapping spectral signatures [Keshava et al. 2002, Mustard et al. 1987]. Beyond spectral data, signal unmixing can apply to any measurements that rely on the combination of multiple components. Accurate component separation is challenging when the specific signal distribution of a given species is unknown or when the sampling coverage is insufficient [McRae et al. 2019, Montag et al. 2016, Iordache et al. 2011].

For multi-dimensional measurements, such as volumetric or spatio-temporal data, the interdependence between different dimensions can be effectively leveraged to create a richer representation that facilitates unmixing. Translating the unmixing task from a signal processing task to a vision analysis one capitalizes on the

connectivity between signals measured at different points, such as neighboring pixels in images. Data-driven approaches excel in feature extraction over multiple dimensions [Goodfellow et al. 2016]. A data-driven unmixing algorithm can learn to recognize the spatial features that are indicative of distinct structures and deduct what parts of different signals should be combined together for an information-rich representation of undersampled pixels.

Unmixing methods for hyperspectral data are often tailored to hyperspectral remote sensing, where the volumes are well-resolved spectrally (≤ 10 nm) but spatially undersampled, as each pixel covers areas of around ten square meters or more [Lin et al. 2015, Wang et al. 2016, Tang et al. 2019, Dong et al. 2020]. In fluorescence microscopy, the unmixing capacity is limited by the number of photons acquired at each pixel and by the brightness of the fluorescent markers and the required image acquisition frequency [Levitt et al. 2020, Andronov et al. 2022]. Combining the photons from adjacent pixels can improve the unmixing performance of multiple markers but reduces the effective spatial resolution [Tardif et al. 2019]. Another application example is the unmixing of sinusoidal signals in multi-mode optical fibers acquired at a sub-Nyquist frequency. When the acquisition is below the Nyquist frequency of the entangled signals, accurately identifying the frequencies of the overlapping signals becomes impossible [Shannon 1949, Nicholson et al. 2008].

In this work, we propose a computer vision inspired unmixing method that applies to various types of undersampled multi-dimensional optical measurements, outperforming signal analysis curve-fitting based methods. Our method, called *Latent Unmixing*, uses learned spatial features to transform the overlapping input contributions to a latent space where they are untangled and can be separated by applying linear bandpass filters directly in the latent space (Fig. 1). It offers a versatile approach to the unmixing problem that can be easily adapted to different distributions and number of unmixed targets. We demonstrate the applicability of our method using three datasets covering distinct use cases in experimental physics.

2 Methodology

2.1 The 3D U-Net Model

The U-Net model [Ronneberger et al. 2015] and its 3D version [Çiçek et al. 2016] are Convolutional Neural Networks (CNNs) that were initially designed for the segmentation of biomedical images. 3D U-Nets have since been proven for analysis tasks in optical microscopy such as the detection of microglial cells in confocal image stacks [Falk et al. 2019], the segmentation of calcium events in fluorescence microscopy videos [Beaupré et al. 2024], of cells in bright-field image stacks [Falk et al. 2019], and of neurites in electron microscopy stacks [Falk et al. 2019]. U-Nets have transcended the field of biomedical image analysis, notably being now employed in diffusion models for image generation [Ho et al. 2020].

We exploit a 3D U-Net [Çiçek et al. 2016] model to map the optical data from the input space, where the signal components are undersampled and overlapping (Fig. 1i), to a latent space where the different contributions are differentiated. The 3D kernels process the three dimensions of an input volume simultaneously, thus combining

essential information from neighbouring pixels and neighbouring time- or spectral-bins (Fig. 1ii). The network has 4 downsampling blocks and 4 upsampling blocks (Suppl. fig. 1). To generalize the model to contexts where the input distribution parameters vary, we developed a conditional paradigm where the parameters that define the distribution of the input volume are embedded to the encoder blocks. The architecture is described in details in Appendix A. As it is standard for U-Nets, the number of dimensions of the input remains unchanged through the layers; the input 3D volume results in a 3D output of dimension $N_i \times N_j \times L$, with N_i , N_j and L coming from the image’s spatial dimensions, and L also being the pixel latent space size.

2.2 Latent space filters

In CNNs, the latent space simplifies the raw input pixel data into an informative representation that is used by the subsequent layers to perform the task [Liu et al. 2019] (Fig. 1iii). Our *Latent Unmixing* method uses this abstract representation of the data to translate the 3D input into a multi-channel 2D output. C predefined bandpass filters are applied to the pixel latent space of the 3D U-Net output to pool this pixel latent dimension into C relative abundance maps (Fig. 1iv). This forces the network to learn a mapping that transforms the input overlapping distributions into a latent space where they do not overlap and can be separated with the predefined bandpass filters. The C relative abundance maps are multiplied to the amplitude of the initial measurement (photon counts or intensity) to obtain a C -channel multiplexed image (Fig. 1v).

Algorithm 1 describes the training process of the *Latent Unmixing* method. The training dataset \mathcal{X} must contain volumetric data samples h^i , along with unmixed ground truth images $x^{i,c}$ for each of C ground truth channels. At each epoch, the latent representation z^i of a batch of data samples is produced by the 3D U-Net model (line 6). The latent vector is processed using C bandpass filters, resulting in the creation of C -channel images where each channel c is the summed signal across filter $bandpass(c)$ (lines 8 and 9). The resulting prediction is normalized along the channel dimension so that each pixel of the original image is associated with a probability of belonging to each channel (line 11). The loss is the mean squared error between the predicted ($\hat{x}^{i,c}$) and ground truth ($x^{i,c}$) multi-channel maps of relative abundances (line 13). The loss is backpropagated to update the weights θ of the network using stochastic gradient descent (line 15). This process is repeated over all batches of training data, and over a number of epochs e^{max} .

3 Experiments

In this work, we demonstrate a signal unmixing method on a variation of the MNIST dataset and on two simulated experimental physics use cases: fluorescence lifetime imaging microscopy (FLIM) and mode decomposition in optical fibers. In all three cases, the input data consists of noisy, undersampled, and overlapping signal distributions that need to be decomposed into multi-channel outputs.

Algorithm 1 Training

```
1: Input:  $\mathcal{X} : \{(h_{(N_x \times N_y \times L)}^i, (x_{(N_x \times N_y)}^{i,c})_{c=1}^C)\}_{i=1}^{\mathcal{I}}$ 
2: Initialize randomly U-Net weights  $\theta^0$ 
3: for  $e = 1, \dots, e^{\max}$  do
4:   for  $i = 1, \dots, \mathcal{I}$  do
5:     // Compute latent representation of  $h^i$ 
6:      $z^i \leftarrow \text{U-Net}(h^i | \theta^e)$ 
7:     // Apply bandpass filters to  $z^i$  and sum
8:      $z^{i,c} \leftarrow \text{bandpass}(z^i, c), \forall c$ 
9:      $\hat{x}^{i,c} \leftarrow \sum_l z_l^{i,c}, \forall c$ 
10:    // Normalize into a probability of belonging to  $c$  (abundance maps)
11:     $\hat{x}^{i,c} \leftarrow \hat{x}^{i,c} \oslash (\sum_c \hat{x}^{i,c})$ 
12:    // Compute loss  $\mathcal{L}^i$ 
13:     $\mathcal{L}^i \leftarrow \frac{1}{N_x \times N_y} \sum_c \sum_{j,k} (\hat{x}_{j,k}^{i,c} - x_{j,k}^{i,c})^2$ 
14:    // Update U-Net parameters
15:     $\theta^e \leftarrow \theta^e - \alpha \nabla_{\theta} \mathcal{L}^i$ 
16:   end for
17: end for
```

3.1 3D MNIST with simulated time dimension

3.1.1 Dataset

We created the 3D-MNIST dataset to benchmark the *Latent Unmixing* method’s performance before demonstrating its potential for real-world applications. Following Algorithm 2, we added a third dimension to the images from the original MNIST dataset [Lecun et al. 1998] to simulate a time-resolved measurement in experimental physics. The added signal in the temporal dimension was characterized by an exponential decay function. Each image i was created by randomly sampling up to three images from classes 4, 8, and 9 from the original MNIST training set [Lecun et al. 1998]. We used this triplet because it has the highest fraction of overlap (Suppl. fig. 2), making it more challenging to untangle for an unmixing algorithm. Random Poisson noise was added as a fourth target channel to simulate background noise in real experimental physics measurements. The generated dataset was parameterized by a signal-to-noise factor R , decay constants for each channel ($\lambda_4, \lambda_8, \lambda_9, \lambda_b$), a time dimension histogram of L bins, and a number of images \mathcal{I} . The digits were independently randomly rotated, flipped and translated (line 17). Images were normalized to the range $[0,1]$ by dividing each image by its maximum value (line 19). To better simulate noisy experimental conditions, we adjusted the normalized pixel values by sampling a random count for each pixel from a Poisson distribution. The sampling parameter is the product of the pixel value and the SNR factor R (as described in lines 21 and 22). For each count, an associated time value was sampled following an exponential distribution parameterized by the decay constant of the channel (line 24). The time values of each individual pixel are converted to a histogram of L bins of fixed width (line 26), where L is the

dimension of the latent space. A background channel was created by randomly sampling values in a Poisson distribution with parameter $\lambda = 5$. A time histogram was built following the same method as for the digits channels (lines 29 to 33). There was a probability 0.5 of picking a digit for each of the classes (lines 9 to 13), such that a training sample could contain 0, 1, 2 or 3 digits among 4, 8 and 9. The volumes (4, 8, 9, background) were summed along the channel dimension to create a mixed volume of dimensions $(28 \times 28 \times L)$ (line 35). The resulting 3D-MNIST dataset consists of 8,000 mixed volumes generated with $R = 5$ and $L = 28$, from which 6,400 randomly sampled volumes were used for training and 1,600 for validation. For testing, the same process was repeated using the test MNIST digits to generate 800 test images with overlapping digits and simulated decay.

The SNR (parameter $R = 5$ in Algo. 2) was chosen such that a simple 2D U-Net could not accurately unmix the digits using the intensity signal only (Appendix C), demonstrating that the time dimension is needed to assign individual counts to the right channel. The decay parameters λ_c were chosen as 10, 5, 3.33 and 2.5 for digits 4, 8, 9 and the background respectively (Fig. 2, top-left).

3.1.2 Training

The *Latent Unmixing* method was trained over the 3D-MNIST dataset to unmix overlapping digits (Fig. 3a) by mapping the input distributions (Fig. 2, top-left) to a pixel latent space where the contributions are well separated to fit the predefined bandpass filters (Fig. 2, Fig. 3b). Four bandpass filters each of width 7, equally spaced along the pixel latent vector of length $L = 28$, were used for this dataset. Training hyperparameters are enumerated in Appendix A.

3.1.3 Results

The 3D-MNIST dataset is designed to have a low signal-to-noise ratio, with an average pixel count of 3.9 for the foreground (non-zero) pixels of individual digit channels and 4.7 for the background channel. The input signal distributions do not provide enough counts to enable the application of curve fitting methods for extracting the relative abundance of up to four components (Suppl. fig. 4). The *Latent Unmixing* model projects the undersampled distributions to the latent space in a way that untangles their relative abundance (Fig. 2, Fig. 3b). Because it is built from a 3D-UNet, the *Latent Unmixing* method combines the spatial features indicative of each digit along with the pixel-wise signals to accurately assign the different contributions. The spatial features indicative of each digit (4, 8, 9) are correctly replicated in the predictions, leading to an accurate pixel-wise reconstruction of each channel (Fig. 3c). The *Latent Unmixing* achieves a Pearson correlation coefficient between true and predicted pixel counts above 0.69 for all channels over the test set (Fig. 3c). To confirm that the time dimension is used by the network to predict the unmixed image, we compared the result with a 2D U-Net trained on the same set of images of overlapping digits without the temporal dimension. The digits can not be recognized in the predicted unmixed images, and the predicted and true counts are not correlated (Appendix C).

We compared the result of *Latent Unmixing* with the established curve fitting approach Maximum Likelihood Estimation (MLE) [Bajzer et al. 1991] to unmix the

Algorithm 2 3D-MNIST dataset generation

```
1: Input: Signal-to-noise factor  $R$ 
2: Input: Exp. distribution parameters  $\lambda_4, \lambda_8, \lambda_9, \lambda_b$ 
3: Input: Length of latent space  $L$ 
4: Input: Number of images to generate  $\mathcal{I}$ 
5: Input: Dataset  $\mathcal{X}$  (MNIST)
6: for  $t = 1, \dots, \mathcal{I}$  do
7:   for  $c \in \{4, 8, 9\}$  do
8:     // Include class  $c$  with a probability of 0.5
9:      $b \sim \mathcal{U}(0, 1)$ 
10:    if  $b > 0.5$  then
11:       $x^{t,c} \leftarrow \emptyset$ 
12:      Skip to next class  $c$ 
13:    end if
14:    // Sampling an image from class  $C_c$ 
15:     $x^{t,c} \leftarrow \text{sample}(\{x^l \in \mathcal{X} \mid y^l = C_c\})$ 
16:    // Transform the image (rot., flips, trans.)
17:     $x^{t,c} \leftarrow \text{transform}(x^{t,c})$ 
18:    // Normalize the image to the range [0,1]
19:     $x_{i,j}^{t,c} \leftarrow x_{i,j}^{t,c} / \max_{l,m}(x_{l,m}^{t,c}), \forall i, j$ 
20:    // Generate noisy version of the digit
21:     $u_{i,j} \sim \text{Pois}(R \times x_{i,j}^{t,c}), \forall i, j$ 
22:     $x^{t,c} \leftarrow u$ 
23:    // Sample  $x_{i,j}^{t,c}$  values from exponential dist.
24:     $s_{i,j,k}^{t,c} \sim \text{Exp}(\lambda_c), k = 1, \dots, x_{i,j}^{t,c}, \forall i, j$ 
25:    // Convert samples to histogram with  $L$  bins
26:     $h_{i,j}^{t,c} \leftarrow \text{hist}(s_{i,j}^{t,c}, L), \forall i, j$ 
27:  end for
28:  // Random background noise
29:   $x_{i,j}^{t,b} \sim \text{Pois}(5), \forall i, j$ 
30:  // Sample  $x_{i,j}^{t,b}$  values from exponential dist.
31:   $s_{i,j,k}^{t,b} \sim \text{Exp}(\lambda_b), k = 1, \dots, x_{i,j}^{t,b}, \forall i, j$ 
32:  // Convert samples to histogram with  $L$  bins
33:   $h_{i,j}^{t,b} \leftarrow \text{hist}(s_{i,j}^{t,b}, L), \forall i, j$ 
34:  // Create the joint histogram
35:   $h^t \leftarrow h^{t,4} + h^{t,8} + h^{t,9} + h^{t,b}$ 
36: end for
37: Return  $\mathcal{X}^G = \{(h^t, (x^{t,c})_{c \in \{4,8,9\}})\}_{t=1}^{\mathcal{I}}$  as generated dataset
```

same test set pixel-by-pixel. We fix the decay constants as the actual λ_c values, and use MLE to fit the relative abundances of the 4 classes (Appendix D). In this context with limited counts per pixel, MLE cannot separate the different contributions from the 4 channels (Table 1, Appendix D) [Bajzer et al. 1991, Enderlein et al. 1997, Enderlein et al. 2001, Sewell et al. 2015]. In our experimental settings, the average

over all pixels of the test set is 5.6 counts per pixel, which is a full order of magnitude below the described limits of MLE [Bajzer et al. 1991, Enderlein et al. 1997].

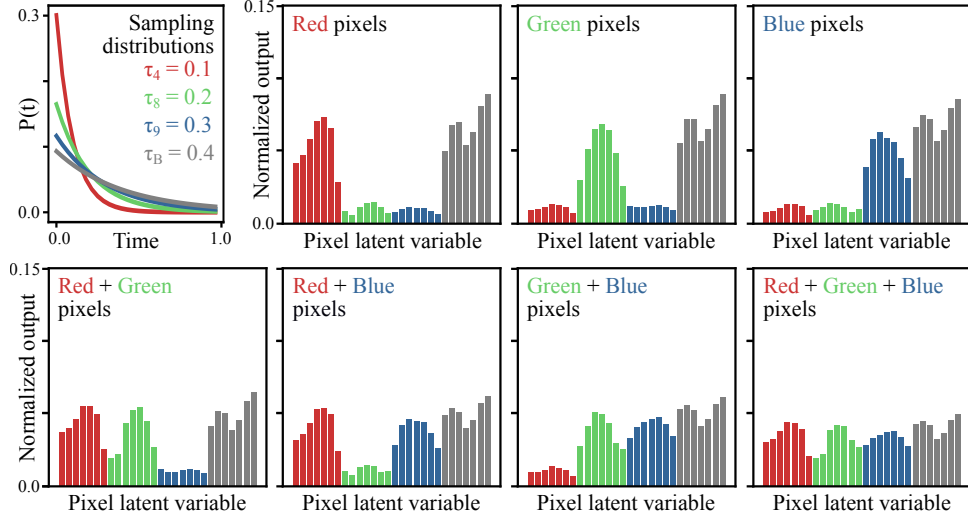


Fig. 2 Top-left: sampling distributions for three-color MNIST with exponential decay parameters $\lambda_c = 1/\tau_c$ of 10, 5, 3.33 and 2.5. Other subfigures: the pixel output value of the pixel latent variable, averaged over all pixels from the simulated test set. Each subfigure represents a different combination of ground truth pixel composition. All pixels contain background noise (gray bins).

	MLE	Latent Unmixing
Channel 4	1.98	0.324
Channel 8	4.76	0.647
Channel 9	4.88	0.553
Background	11.69	1.01

Table 1 Mean squared error (MSE) between true and predicted counts using MLE and *Latent Unmixing* over the test set of the 3D-MNIST dataset (N=800 images).

3.2 Fluorescence lifetime microscopy

In recent years, major developments have been made to achieve multiplexed fluorescence microscopy, enabling the characterization of cellular and molecular interactions between multiple partners [Frei et al. 2022, Valm et al. 2017, Barroso et al. 2023, Tardif et al. 2019]. FLIM uses the arrival time of fluorescence photons to assign them to specific fluorophores or to measure environmental changes in biological samples [Dong et al. 2003, Becker et al. 2012]. The fluorescence decay follows an exponential probability distribution characterized by the parameter τ corresponding to the

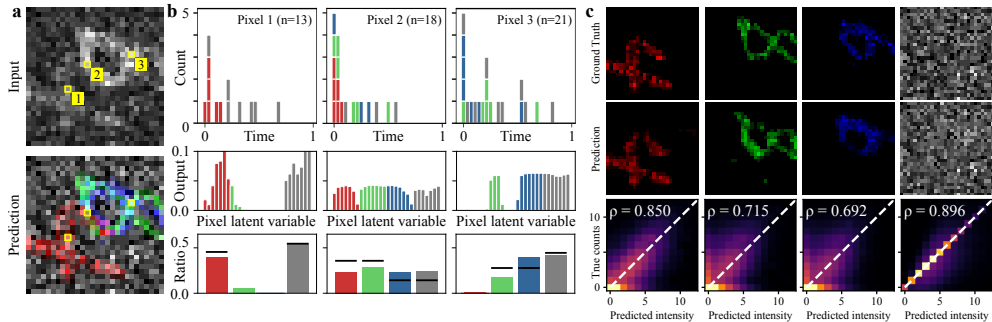


Fig. 3 Latent unmixing on the MNIST Dataset. **a**, Input intensity image (top) and the corresponding unmixed 4 channel prediction (bottom). **b**, The input distributions (top) and pixel latent variable, before (middle) and after (bottom) applying the bandpass filters on the latent space. Results are shown for the three pixels highlighted in **a** (yellow boxes). The black horizontal lines (bottom) represent the relative abundance of each channel in the ground truth image. **c**, Channel-wise unmixing results on the test set, with ground truth (top), *Latent Unmixing* prediction (middle), and correlation matrices between true and predicted photon counts (bottom) ($N=800$ images, 627,200 pixels). Dashed white lines show a perfect correlation with a slope of 1. Colormaps are square-root normalized and scaled to the second maximum of each matrix. ρ is the Pearson correlation coefficient between the ground truth and predicted counts for each channel.

fluorescence lifetime [Berezin et al. 2010]. The fluorescence lifetime is a unique photo-physical property of each fluorescent molecule, which is used in FLIM to differentiate between fluorescence emitters [Dong et al. 2003]. Despite careful selection of fluorophores with distinct fluorescence lifetime, overlapping exponential distributions pose challenges for signal unmixing [Digman et al. 2008]. This is particularly difficult with low photon counts (less than 100 photons/pixel) or when multiple fluorophores coexist at the same location [Smith et al. 2020, Nasser et al. 2022, Tardif et al. 2019]. For live-cell imaging, where photobleaching and sample movement should be minimized, FLIM measurements are generally associated with low photon-counts (<25 photons per pixel [Ahmed-Cox et al. 2022]). Similarly, low photon-counts are observed for Stimulated Emission Depletion (STED) super-resolution microscopy combined with FLIM [Bucker et al. 2011, Sun et al. 2017, Tardif et al. 2019, Tortarolo et al. 2019, Gonzalez et al. 2022]. Development of analytical methods that can be applied to limited photon budgets in multiplexed FLIM imaging would have an important impact in the field, allowing to increase sampling rates for live-cell imaging or to resolve nanostructures in super-resolution microscopy.

3.2.1 Related work

Different signal unmixing approaches have been proposed specifically for FLIM data analysis. MLE is commonly used for unmixing FLIM data, but it requires high photon counts for an accurate estimation of the relative abundance of each emitter even for known and well separated lifetime values (>300 photons, Appendix F) [Bajzer et al. 1991, Enderlein et al. 1997]. Phasor analysis utilizes graphical representations to simplify the identification of composite lifetimes without requiring

iterative fitting [Digman et al. 2008, Ranjit et al. 2018]. Still, emitters separation in FLIM analysis is not accurate for low photon counts (<300) and for more than 3 fluorescent species when using either the phasor or MLE approaches (Appendix F and G) [Digman et al. 2008, Chessel et al. 2013, Chen et al. 2023, Rowley et al. 2011].

Recently, machine learning based approaches have been proposed for FLIM data analysis [Mannam et al. 2020, Zang et al. 2023]. The *Fluorescence lifetime imaging network* (FLI-Net) [Smith et al. 2019] is a 3D-CNN that takes as input a 3D FLIM volume (x,y,t) where each pixel is characterized by photons sampled in an exponential distribution. FLI-Net assigns a mean lifetime to each pixel rather than unmixing the input image. The FLIM analysis method based on Generative Adversarial Network (GAN) Estimation (flimGANE) [Chen et al. 2022, Chen et al. 2023, Sun et al. 2024] uses a GAN to generate high-quality FLIM images based on photon-starved (50-200 photons per pixel) measurements. Both FLI-Net and flimGANE models are limited to two components unmixing, since their architectures are both designed for three outputs: lifetime values τ_1 and τ_2 , and relative abundance A .

Our proposed approach addresses the challenge of unmixing more than two independent fluorophores in FLIM data, tailored for contexts where the photon counts per pixel aligns with that observed in STimulated Emission Depletion (STED) super-resolution microscopy or time-lapse confocal microscopy (< 100 photons/pixel).

3.2.2 Dataset

The FLIM-STED training dataset consists of 30 real microscopy images of fixed neurons from primary cell cultures and acute brain slices. Images of different combinations of four neuronal proteins tagged with fluorescent markers were acquired over large fields of view (width between 8 and 16 μm and height between 45 and 65 μm) (Appendix E). The signal from each fluorescent marker was spectrally separated to obtain ground truth unmixed images with four independent channels. The number of channels for the ground truth dataset is limited by what can be routinely spectrally separated with a standard STED microscope and currently available antibodies (Appendix E). This is not a limitation of the *Latent Unmixing* method, which can be adapted to any number of target channels.

Prior to training, the images were cropped into 256×256 pixels crops using a sliding window with steps of 128 pixels. Crops were kept in the training set if the mean photon count of each of the 4 channels was at least 1 photon per pixel. This operation resulted in a set of 1132 crops for training. To augment the data during training, samples were further randomly cropped to a size of 64×64 pixels, randomly flipped and rotated, channels were permuted, and up to two channels were removed. The time dimension was created during training by first sampling one lifetime value $\tau_1 \sim \mathcal{N}(1.5, 0.5)$ for the first non-zero channel, then adding $\delta \sim \Gamma(1, 0.5)$ for each subsequent non-zero channel. The δ value is clipped above 0.2 to insure a minimal distance between lifetime values of 0.2 nanoseconds. Random arrival time values for each photons are sampled in an exponential decay curve parameterized by the channel’s lifetime. We chose to pick lifetime values in the range from 0 to 6 nanoseconds because this range includes the majority of the commercially available dyes [Frei et al. 2022, Berezin et al. 2010]. Training a model on a predefined

set of lifetime values would not capture the true measured distributions of fluorescence lifetime in a real sample, especially for live-cell FLIM or FRET-FLIM experiments [Peter et al. 2005].

For testing, the test set was created from 12 4-channel intensity images that were not used for training. The time dimension simulated for the test images was generated using different parameters to quantify the performance of the method over different variables, described in the results section and in Appendix I.

3.2.3 Training

The FLIM-STED unmixing task serves as a demonstration of the *latent unmixing* method in a real experimental setting. For multi-channel FLIM-STED, channel separation is challenging at low photon counts (< 50 photons per pixel), for more than two fluorescent markers, and for small lifetime differences between the emitters (< 1 ns). To ensure the generalizability of the model over different spatial features, we trained a conditional U-Net with a conditioning vector inspired by the denoising diffusion model [Ho et al. 2020] (Fig. 4b). For conditional unmixing, the U-Net takes as input a vector $\mathcal{T} = [\tau_1, \tau_2, \tau_3, \tau_4]$ in addition to the volumetric image to unmix. For images with less than 4 channels, the empty channels are represented by $\tau = -1$. \mathcal{T} is projected to encoding blocks by passing through two learnable fully-connected layers both with 64 nodes, with a GELU activation in-between, and a SiLU activation afterwards (Suppl. fig. 1). The learned representation then goes through a third fully-connected layer with an output size corresponding to the number of filters of each encoding block (128, 256, 512 and 1024). The values output by this fully-connected layer are then used to scale and shift the input of each encoding block [Ho et al. 2020]. The *Latent Unmixing* model was trained on the FLIM-STED dataset to map the input volumes of depth $L = 40$ time-bins of width 0.5 ns (Fig. 4a) to a latent space of the same length, on which 4 bandpass filters equally spaced and of equal width of 8 were applied (Fig. 4c,d,e), similarly to the 3D-MNIST experiment. Unlike the 3D-MNIST dataset, the FLIM-STED dataset does not include an independent background channel with a specific lifetime. To create the background channel, we simply assign all pixels with a count below 4 photons to the background. Because background photons have an unknown lifetime distribution, we assign the 6 bins at the intersection between channel-filters and the 2 bins at the extremities of the latent vector to a fifth channel corresponding to the background photons (Fig. 4c,d,e). The first bandpass filter covers the elements 2 to 9, the second 12 to 19, the third 22 to 29, the fourth 32 to 39, and the background channel is created from the remaining elements, i.e. element 1, 10, 11, 20, 21, 30 and 31. This allows the network to allocate signal to intersecting elements for pixels with insufficient photons to be accurately classified as any channel other than the background.

3.2.4 Results

The 12 test images were each split into 256×256 crops using a sliding window with steps of 128 pixels resulting in 800 testing crops. Each crop was processed by the *Latent Unmixing* model independently. The predicted crops were recombined to generate the

full field of view image by using the central 128×128 region of each prediction without overlap, thereby eliminating potential border effects.

Generalizability to 2-, 3-, and 4-channels unmixing

The vector \mathcal{T} encoded into the U-Net makes the network adaptable to different numbers of emitters between 2 and 4. The projection of the input volume in the latent space adapts to the number of emitters dictated by \mathcal{T} (Fig. 4a-b). When the 4 values of \mathcal{T} are positive, the network decodes the input into 4 channels (Fig. 4c). Selecting the last value of \mathcal{T} to -1 excludes signal from the last bandpass filter, yielding a three-channel image (Fig. 4d). Fixing the last two values of \mathcal{T} at -1 similarly limits the signal to two channels (Fig. 4e). An input volume can be unmixed into 2-, 3-, or 4-channels using a single 3D U-Net trained once, simply by changing the values of \mathcal{T} given as input along with the FLIM volume (Fig. 4 and Fig. 5).

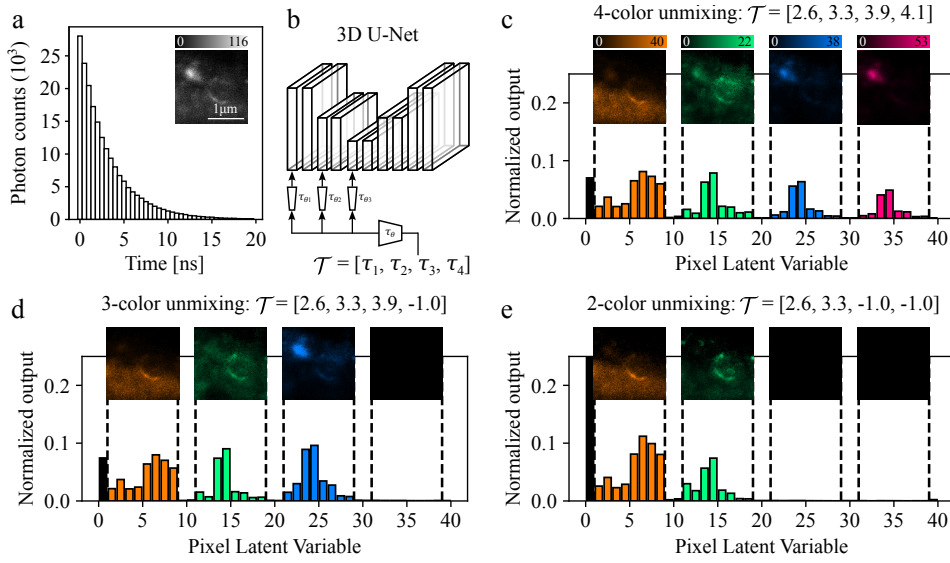


Fig. 4 **a** Example input crop with the time distribution of *all* pixels in the crop. **b** The network used for conditional unmixing. The vector \mathcal{T} contains the lifetime values of the 4 emitters in the sample, in ascending order. If the sample contains less than 4 emitters, the extra lifetime values are replaced by -1 and ordered last. τ is encoded by a multilayer encoder τ_θ and layer specific encoders $\tau_{\theta 1}$, $\tau_{\theta 2}$, and $\tau_{\theta 3}$. **c** Output for 4-color unmixing with $\mathcal{T} = [2.6, 3.3, 3.9, 4.1]$. **d** Output for 3-color unmixing with $\mathcal{T} = [2.6, 3.3, 3.9, -1.0]$. **e** Output for 2-color unmixing with $\mathcal{T} = [2.6, 3.3, -1.0, -1.0]$. Lifetime values are chosen to reflect the theoretical lifetimes of the fluorescent dyes used in this specific experimental context (ATTO 490LS, STAR635P, Alexa Fluor 594, Alexa Fluor 488). The displayed colorscale of each individual image is the 99.5th percentile of the 4-color prediction. Images show 4 fluorescently labeled neuronal proteins. Orange: Microtubule-associated protein 2c (MAP2c), Green: Postsynaptic density protein 95 (PSD95), Blue: Vesicular glutamate transporter 1 (VGLUT1), Pink: RNA-binding protein fused in sarcoma (FUS).

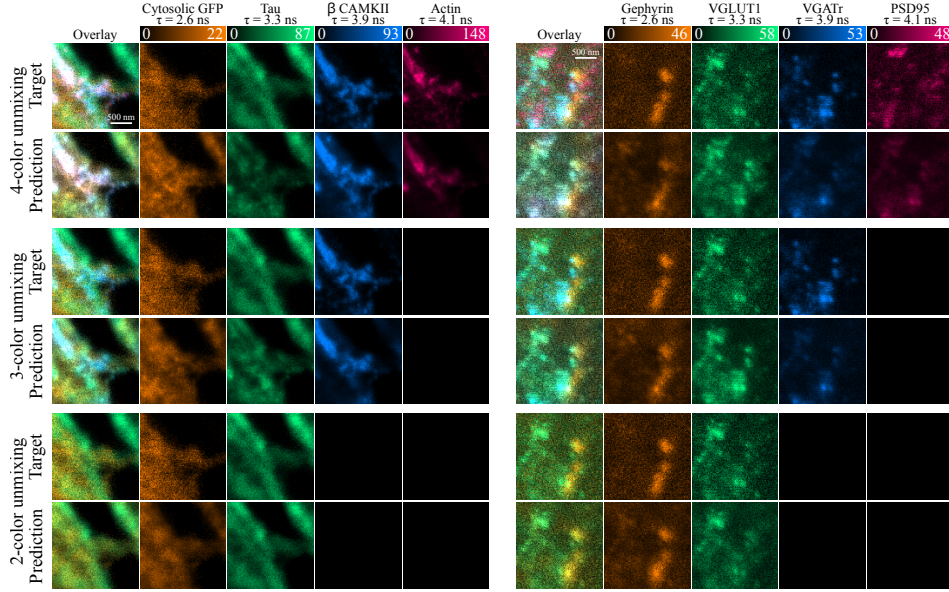


Fig. 5 Example crops from the test set with simulated lifetime for two sets of fluorescently labeled proteins (left: cytosolic Green Fluorescent Protein (GFP), Tau, β CaMKII and F-Actin in fixed cultured hippocampal neuronal cultures; right: Gephyrin, VGLUT1, VGAT and PSD95 in fixed acute brain slices). The ground truth has either 4 (top), 3 (middle) or 2 (bottom) channels to unmix, showcasing that the same model can be applied for different number of emitters. Color scales at the top show min-max display values and correspond to the 99.5th percentile of the ground truth channel.

The generalizability of the *Latent Unmixing* method over 2-, 3-, and 4-channels unmixing was evaluated over a test set of 264 FLIM images with 2, 3, or 4 simulated emitters produced from 12 4-colors intensity images (Appendix I). For interpreting the performance over the foreground pixels, a foreground mask was computed using a triangle thresholding approach applied independently to each channel [Zack et al. 1977]. For very low photon counts (0 to 5 photons per foreground pixel), the *Latent Unmixing* method achieves a median Pearson correlation coefficient of 0.85 ± 0.10 (mean \pm standard deviation) for 2-channel, 0.79 ± 0.10 for 3-channel, and 0.72 ± 0.05 for 4-channel unmixing (Fig. 6). For slightly higher counts (5 to 10), the performance jumps to 0.95 ± 0.03 for 2-channel, 0.90 ± 0.06 for 3-channel, and 0.86 ± 0.08 for 4-channel, and is then relatively stable for up to the maximum mean count (35 to 40 photons/pixel), reaching 0.992 ± 0.002 for 2-channel, 0.96 ± 0.05 for 3-channel, and 0.950 ± 0.006 for 4-channel unmixing.

The *Latent Unmixing* method outperforms the phasor analysis method over the test set for 3- and 4-channels unmixing for all combinations of lifetime values tested. For photon counts that are realistic of what is expected from experimental acquisitions (counts in the range 0 to 50 photons per pixels), the projection of the pixels to the phasor plot space is too noisy for the abundance to be accurately predicted, resulting in noisy and unreliable unmixed channels (Fig. 7 and Fig. 8). With the *Latent Unmixing*

method, the spatial features derived from the neighborhood of each pixel helps reach more accurate predictions, achieving a Pearson correlation coefficient (mean \pm STD) of 0.88 ± 0.08 over the 4 channels of the 12 test images with simulated lifetime values of 1.0, 2.0, 3.0 and 4.0 ns, compared to 0.52 ± 0.03 using the phasor analysis method.

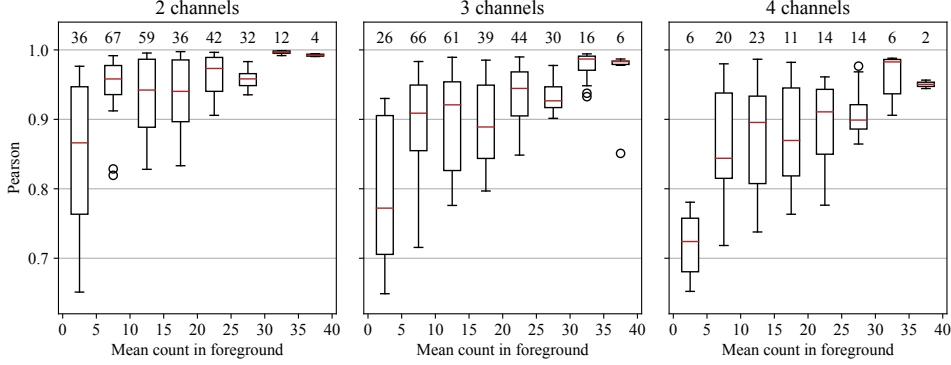


Fig. 6 Pearson correlation coefficient between the pixel counts in the ground truth and the latent unmixing prediction for 2- (left), 3- (middle) and 4-channel (right) unmixing. Images are binned into ranges of 5 counts per pixels over the foreground pixels of the image. The numbers above the boxes are the number of channels in each distribution. $N=288$ for 2-channels, $N=288$ for 3-channels, and $N=96$ for 4-channels (Appendix I).

Robustness to low-photon counts

A key aspect of the *Latent Unmixing* method is that the information from neighbouring pixels is processed simultaneously by the 3D convolutional kernels, which should lead to more accurate unmixing for low-photon counts than single-pixel methods like the phasor analysis. Since the phasor analysis method can not accurately unmix more than two emitters in the photon counts range we operate at (Appendix G), the quantitative comparison between the two methods concentrates on the 2-channel case. The quantitative analysis covers a test set of 168 2-channel FLIM images simulated from 12 real intensity STED images and 14 combinations of two lifetime values (Appendix I). For all $\Delta\tau$ tested, the relative error between the true and predicted counts per channel for each pixel decreases when the photon count increases (Fig. 9). For lifetime differences below 2.2 ns, *Latent Unmixing* outperforms the phasor analysis method for both the image-wise Pearson correlation coefficient (Fig. 10) and the pixel-wise relative error (Fig. 9). The effect is more pronounced for lower photon counts. For all lifetime differences covered (0.2 - 2.8 ns), the performance of *Latent Unmixing* is more stable than the phasor approach for counts below 50 photons/pixel.

Robustness to close lifetime values

Finding pairs of fluorophores that have distant lifetime values can be a challenge for biological applications. The ability to correctly unmix two channels with lifetime

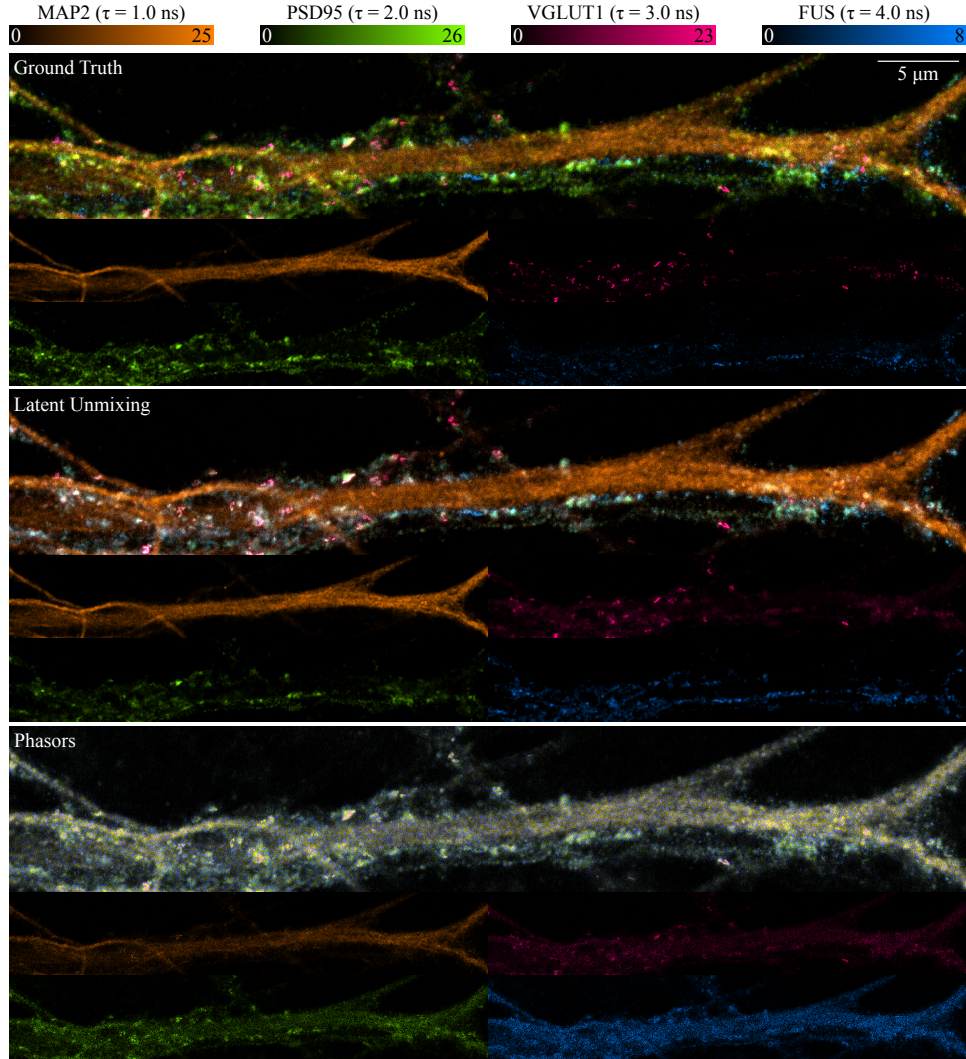


Fig. 7 4-channel unmixing with the *Latent Unmixing* and the phasor analysis methods. Photon counts are representative of real acquisitions, as they are taken directly from the acquired intensity confocal and STED images. All colormaps are scaled from 0 to the 99.9th percentile of the ground truth channels, indicated by the colorbars. Lifetime values (1.0 ns, 2.0 ns, 3.0 ns and 4.0 ns) are chosen to serve as an easy case ($\delta\tau = 1.0$ ns for all channels), while remaining in the realm of possible lifetime values with current commercially available dyes. Refer to suppl. fig. 7 and 8 for more qualitative examples over different protein combinations.

values that are close apart (<1 ns) is therefore a valuable advantage for an unmixing method. Our *Latent Unmixing* method shows better robustness to close lifetime than the phasor analysis method (Fig. 10), achieving a Pearson correlation of $\rho = 0.86 \pm 0.11$

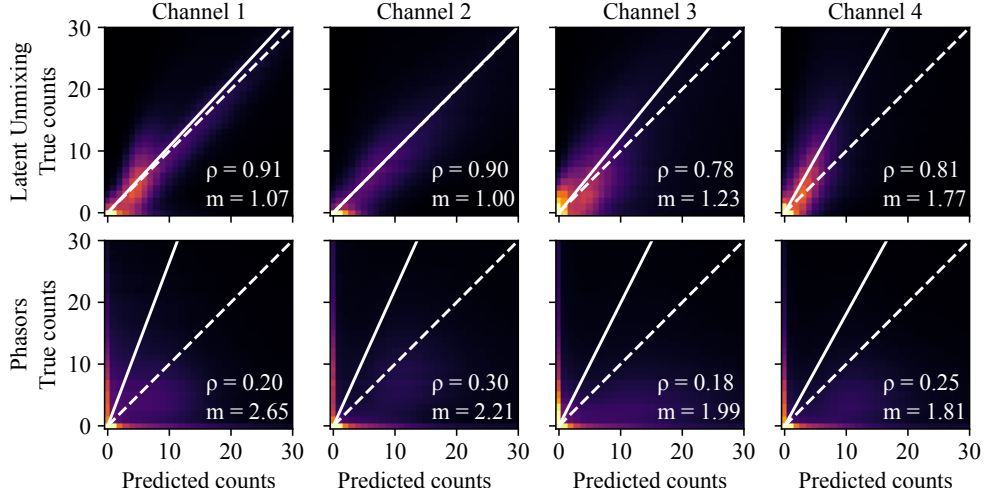


Fig. 8 Correlation matrices obtained over the 12 images from the test set, simulated with lifetime values of 1.0, 2.0, 3.0 and 4.0 ns, with *Latent Unmixing* (top) and Phasor analysis (bottom). ρ is the Pearson correlation coefficient, m is the slope of the linear regression between predicted and actual counts. Dashed lines show a perfect correlation with a slope of 1. Colormaps are square-root normalized and scaled to the second maximum of each matrix.

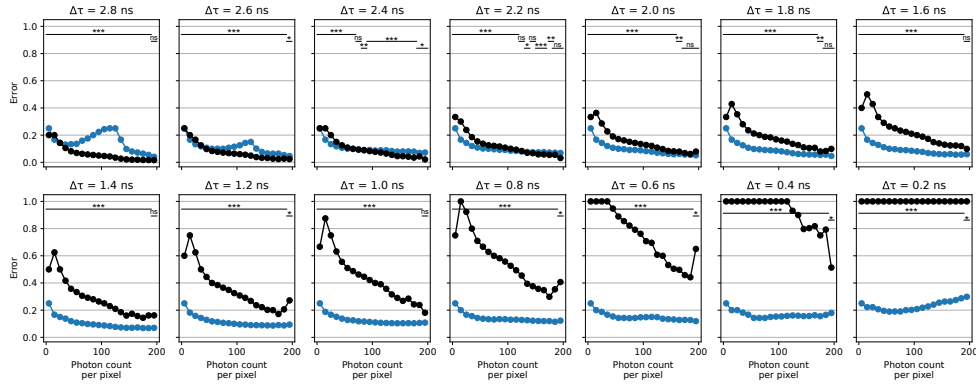


Fig. 9 Influence of the lifetime difference and the photon counts for 2-channel unmixing. Median relative error for the predicted counts of all pixels above 3 photons/pixels of the test images, using the predictions of the phasor analysis (black) and the *Latent Unmixing* (blue) methods. Pixel counts are binned in 10-count intervals. From left to right and top to bottom, the difference between the two lifetime values decreases from 2.8 ns to 0.2 ns. For large differences, both methods perform similarly. For smaller differences (≤ 1.6 ns), *Latent Unmixing* outperforms the phasors approach, with the difference between the two methods increasing for decreasing photon counts. Statistical analysis: the two distributions come from populations with the same median (refer to suppl. sec. 4.5), *** : $p \leq 0.001$, ** : $p \leq 0.01$, not significant (ns): $p > 0.05$.

(mean \pm STD, N=24) for lifetime values only 0.2 ns apart, compared to the phasor

analysis method that achieves only $\rho = 0.68 \pm 0.06$. In the 2-channel unmixing context, differences of 2.4 ns and above lead to similar performances for both approaches. In practice, a lifetime difference above 2.2 ns is rarely achievable given the finite number of fluorescent dyes available commercially.

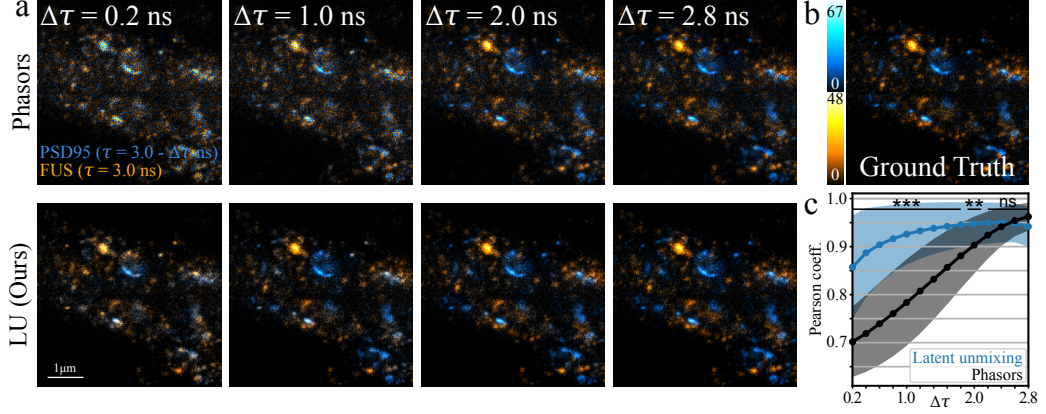


Fig. 10 **a** Image crop from the FLIM-STED test dataset comparing the performance of the phasor analysis and our *Latent Unmixing* (LU) method as a function of the difference between the lifetime values of both channels ($\Delta\tau$). **b**, Ground truth. The colorbars show the display range for all images in **a** and **b**. **c**, Pearson correlation coefficient computed over the images of the test set using the *Latent Unmixing* and the phasors methods. Each point is the mean computed over the 2 channels of the 12 test images ($N=24$), and the shaded region is the standard deviation. See Suppl. Fig. 10 for an additional example. Statistical analysis null hypothesis: the two distributions have the same mean (refer to Appendix K), *** : $p \leq 0.001$, ** : $p \leq 0.01$, not significant (ns): $p > 0.05$.

3.2.5 Unmixing real FLIM measurements

The *Latent Unmixing* method is trained on real images supplemented with simulated lifetime values data. The simulated data can cover any range and combinations of lifetime values, enabling the training of a general model that can be applied to any pair of lifetime values. We applied the same *Latent Unmixing* model trained on the simulated FLIM-STED dataset on real FLIM measurements (Fig. 11) with different lifetime values, photon counts, and biological structures; all using the same general model. The real measurements require only simple preprocessing steps to fit the format of the simulated training data. The Instrument Response Function is first removed by shifting the exponential distribution such that its maximum is at the 0-value, commonly known as tail-fitting [Zhang et al. 2016]. The time measurement is then binned into 40 intervals of 0.5 ns to match the training data.

To define \mathcal{T} to make the predictions, control samples with only one tagged protein were imaged. The lifetime value of the protein was defined from the MLE of the parameters of the exponential distribution over all pixels in the control image. For each

protein, 12 to 20 control images were used and the measured lifetime was averaged over all control images (Suppl. Table 9). The sum of all collected photons over all pixels of a control image is between 6.7×10^4 and 3.4×10^6 counts, ensuring MLE is a suitable method for lifetime estimation.

To validate the predictions, the first test is done using pairs of control images with a single tagged protein summed together along the time dimension, so that the two control images can be used as perfect ground truth images (Fig. 11). The qualitative results show that *Latent Unmixing* can unmix real FLIM measurements, even though it was trained only with a simulated time dimension sampled from simple exponential decay distributions. The lifetime conditioning also ensures the method is adaptable across a range of lifetime values and can therefore be applied to various combinations of emitters without requiring any retraining or fine-tuning. For emitters with really close lifetime values (bottom example, CF594 attached to two different proteins, $\Delta\tau = 0.19$ ns), the prediction of the *Latent Unmixing* method shows considerable cross-talk between channels, showcasing the limits of the method; the simulated FLIM-STED training dataset was defined such that two channels could not have a lifetime difference under 0.2 ns. The method is then tested over real FLIM measurements with two tagged proteins (Fig. 12). Even though the ground truth is not available to compare the predictions, the unmixing results obtained with *Latent Unmixing* more closely resembles the morphology of synapses, with well separated pre- and post-synaptic densities, as shown in the selected zoomed-in regions. The phasor analysis method leads to noisier predictions with more overlap between channels.

3.3 Mode decomposition in multi-mode fibers

Microscopy is not the only experimental context where measurements are noisy or undersampled. All physical measurements are expected to be contaminated with a certain amount of noise that is either generated from the instrument, from external sources, or from random statistical fluctuations. Measurements are generally limited in frequency, which can also lead to noisy or under-defined signals. To verify whether the *Latent Unmixing* method can be applied to other types of measurements and temporal distributions, we developed a use-case for the decomposition of overlapping propagating modes from the intensity signal measured at the output of a multi-mode optical fiber. This experimental context differs from the lifetime measurements of fluorescence, allowing for the evaluation of the generalizability of our method.

3.3.1 Related work

Multi-mode optical fibers support the propagation of multiple simultaneous light modes [Gloge et al. 1972]. Spatially and spectrally resolved (S^2) imaging [Nicholson et al. 2008] is a measurement commonly used for characterizing how light travels through multi-mode optical fibers. By measuring the spatial distribution of the intensity at the output of the fiber for a range of laser wavelengths, the propagation modes of the light through the fiber can be characterized. The measurement at the fiber output is not a simple linear combination of each distinct mode due to interference. When multiple modes propagate through the fiber, the intensity oscillates

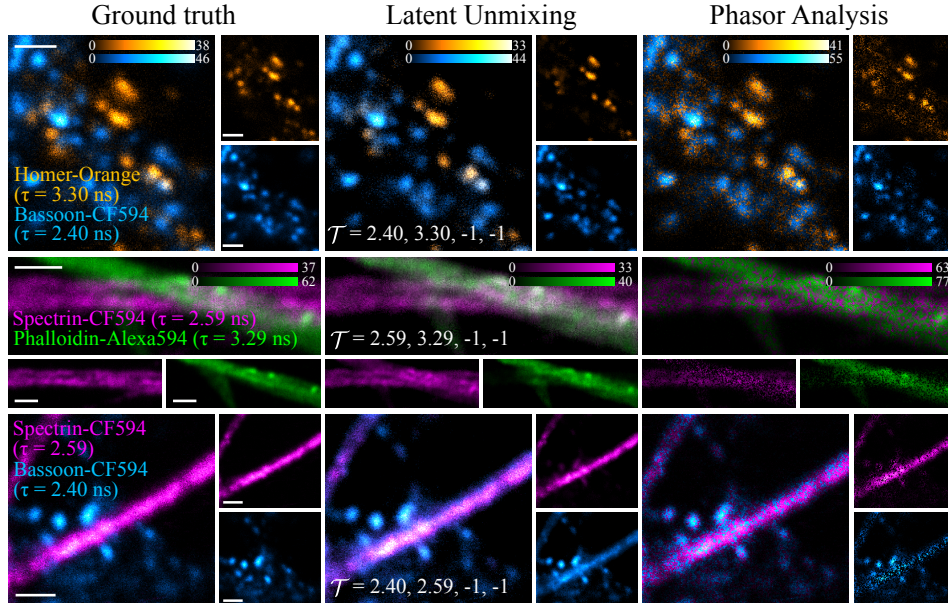


Fig. 11 Results on FLIM measurements obtained with phasors and *Latent Unmixing* for two pairs of fluorescent dyes (Orange/CF594, CF594/Alexa594, and CF594/CF594) with different average lifetime values (3.30 ns/2.40 ns, 2.59 ns / 3.29 ns, and 2.40 ns / 2.59 ns). The 2-channel mixed images are generated by adding together two 1-channel control images, so that the results can be compared with a perfect ground truth. The colormap for each channel is scaled to its own maximum intensity. Scale bars = 1 μm .

as a composite of sinusoidal functions, each corresponding to the interaction between pairs of modes [Nicholson et al. 2008].

In an S^2 measurement for which the sampling frequency is above the Nyquist criterion, the measured oscillations allow to separate each mode with a Fourier transform based method [Nguyen et al. 2012] or by principal component analysis (PCA) [Quiquempois et al. 2021, Seigny et al. 2014]. Other methods exist to achieve real-time mode decomposition from a single image [Huang et al. 2015, An et al. 2020, Manuylovich et al. 2020], but they all require the *a priori* knowledge of the spatial distribution of each mode.

To our knowledge, no method for mode decomposition in multi-mode fibers allows to separate modes with unknown spatial distributions and successfully retrieve their contribution in measurements using a sub-Nyquist sampling rate.

3.3.2 Dataset

The S^2 -MMF dataset consists in simulated images of the intensity measured at the output of optical fibers for different input wavelengths [Nicholson et al. 2008]. The simulated measurements have two spatial dimensions (2D images of the light distribution at the fiber output, fig. 13a) and one spectral dimensions (Fig. 13b). The

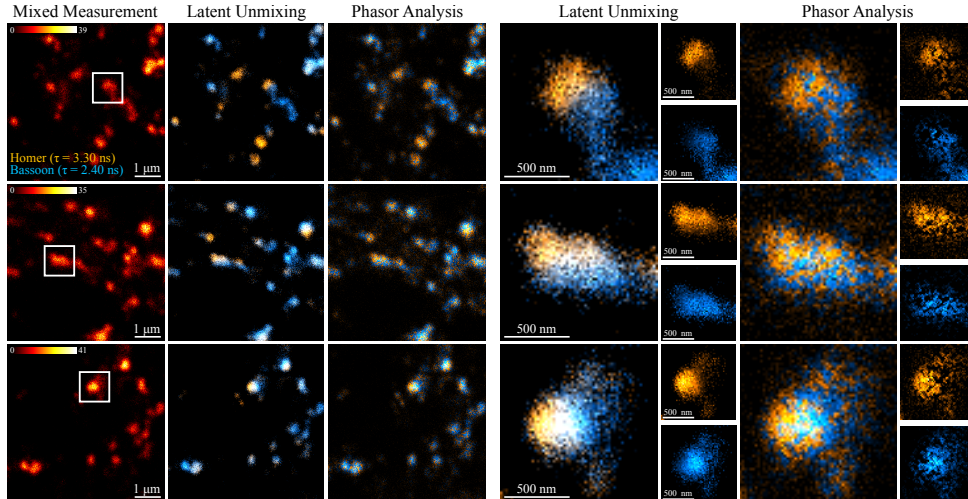


Fig. 12 Results on real FLIM measurements with phasors and *Latent Unmixing* for real FLIM measurements of the synaptic protein pair Homer-Orange (orange) and Bassoon-CF594 (blue). The colormap for each channel is scaled to its maximum intensity. Images on the right are zoomed in regions identified by the white boxes in the mixed intensity images.

dataset was computed with previously described equations [Quiquempois et al. 2021]. A vector finite difference mode-solver [Fallahkhair et al. 2008] was used to find mode properties around 1550 nm for various index profiles and fiber geometries. All fibers simulated in the dataset support up to 6 modes. The mode spatial distribution and effective index dependency on wavelength (dispersion) were taken into account. For all data samples, we considered a spectral range of 6 nm for a fiber length of 5 m. The dataset includes simulated measurements with various combinations of up to 6 propagating modes, different fiber geometries (step-index with varying numerical apertures and core size, GRIN, W-type, H-type and a realistic step-index geometry with a central dip), and different resulting mode-specific intensities (\mathcal{F}). We used 1500 randomly generated mode combinations to train the network and 175 for testing.

3.3.3 Training

The S²-MMF dataset is used to test if *Latent Unmixing* can generalize to other types of distributions than exponential decays; here, interfering sinusoidal signals with varying spatial intensities. For every single pixel, the sampling rate is below the Nyquist frequency, which is the minimal frequency of acquisition that would allow the application of Fourier-based processing methods. By applying our approach to the S²-MMF volumes, the correlation from multiple pixels provides information to find the unknown intensity and spatial distribution of multiple coherent electromagnetic modes propagating simultaneously in a given optical fiber. The *Latent Unmixing* method was trained to map the input data to a latent space of length 60, where 6 bandpass filters of width 10 are applied to separate the space into 6 target modes (Fig. 13c). Only the

volumetric simulated measurement is given as input to the network; the model is not conditioned over the characteristics of the simulated optical fiber. The ground truth is the relative spatial intensity of each mode at the central wavelength (1550 nm), and the channels are ordered in ascending mode order.

3.3.4 Results

The results obtained with the S^2 -MMF experiment demonstrate that the *Latent Unmixing* method can untangle the different signal contributions from sub-Nyquist measurements (Fig. 13). We first evaluate the relative abundance maps of each mode. *Latent Unmixing* correctly recreates the spatial features of each mode, which varies in function of the geometric parameters of the simulated fiber (Fig. 13d, Suppl. Fig. 13). The correlation between the pixel-wise values of the ground truth and predicted pixels is above 0.778 for all modes (Suppl. Fig. 12, Table 3). During training and at inference time, the model is not conditioned over the geometric characteristics of the simulated optical fiber; the spatial distribution of the modes is predicted directly from the input signals. This result makes the *Latent Unmixing* method more generally applicable than methods that require the spatial distributions to be known before-hand to correctly retrieve the relative intensity of each mode [Huang et al. 2015, An et al. 2020, Manuylovich et al. 2020].

Secondly, we also explore the results over the mode-wise relative intensity, or the fraction of the total intensity that is propagated through each mode. This is one of the aspects analyzed when using S^2 measurements to characterize optical fibers [Nicholson et al. 2008]. The relative intensity is obtained by summing the pixel values of the predicted image of each mode, and dividing by the pixels values over all 6 predicted modes. The predicted and ground truth fractions of intensity correlate (Table 2, Fig. 14) over all numbers of propagating modes. There are more errors (outliers from the diagonal in Fig. 14) for smaller numbers of modes in the mixture (2 or 3 modes) than for higher numbers of modes (4, 5 or 6), because the model tends to assign some relative intensity even to non-propagating modes. This is a drawback from the fact that our method does not require knowledge about the spatial distribution of the modes, the number of modes in the mixtures, or the geometric parameters of the optical fiber. For an experimental context where those parameters are completely or partially known, a conditioning branch (Suppl. fig. 1) could be added to improve the performance, as it was done for the FLIM-STED unmixing experiments.

4 Discussion and conclusion

Linear unmixing methods exploit the fact that the signal measured at each pixel is a linear combination of each components' specific signature weighted by its relative abundance [Keshava et al. 2002]. When the signature is known, the relative abundance parameters can be retrieved using estimation algorithms such as least squares fitting methods [Shimabukuro et al. 1991, Heinz et al. 2001] and MLE [Bajzer et al. 1991]. With these methods relying on curve fitting algorithms, the sampling rate must be high enough to ensure that enough data points are collected for the curves to be accurately estimated from the raw data. Another linear unmixing approach, the

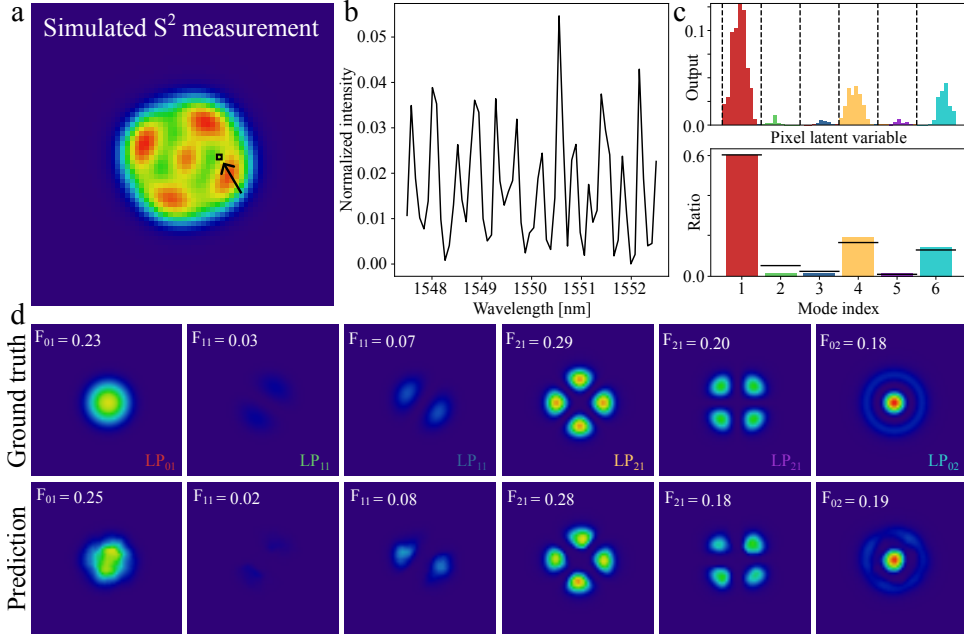


Fig. 13 **a**, Input spatial distribution of a test S^2 measurement. **b**, Spectral distribution of the highlighted pixel. **c**, Top: raw distribution of the same pixel in the latent space. Bottom: distribution of intensity pooled into 6 classes for the 6 modes, with black lines indicating the ground truth proportion of intensity in each mode. **d**, Ground truth (top) and prediction (bottom) for the 6-mode decomposition of the test data shown in **a** and **b**. More examples of predicted spatial distributions are shown in Suppl. Fig. 13.

Number of modes	Pearson ρ
1 mode	1.000
2 modes	0.781
3 modes	0.870
4 modes	0.970
5 modes	0.947
6 modes	0.675

Table 2 Pearson correlation on the relative intensity of the modes F obtained on the test set for different numbers of propagating modes ($N=175$ total simulated measurements).

Mode index	Pearson ρ
Mode 1	0.869
Mode 2	0.778
Mode 3	0.822
Mode 4	0.813
Mode 5	0.801
Mode 6	0.918

Table 3 Pearson correlation coefficient of the relative intensity of each pixel computed over the test set ($N=175$ simulated measurements, 716,800 pixels).

phasor method [Liao et al. 2014], translates the raw measurements to a 2D phasor space where the distributions are represented by the real and imaginary components of their Fourier transform [Digman et al. 2008]. This representation then allows to

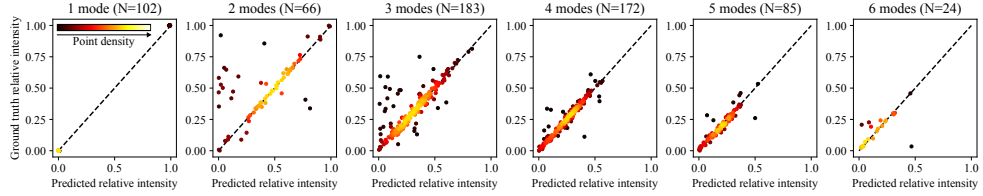


Fig. 14 Correlation between the target and predicted intensity over different mixtures of propagating modes. Dashed line is the perfect correlation with a slope of 1. Points are color-coded by the spatial density of points, estimated by kernel-density with Gaussian kernels, to show the higher density over the diagonal. For numbers of modes above 1, points for which the ground truth channel is empty are omitted for clarity (see Suppl. fig. 11 which includes all points).

estimate the relative abundance of different components through a linear interpolation, knowing the phasor coordinates of individual components obtained through control measurements [Rahim et al. 2022, Gonzalez et al. 2022, Stringari et al. 2011, Vallmitjana et al. 2022]. These methods approach the task of unmixing as a signal processing problem, treating each pixel independently. This limits the amount of information utilized because it fails to consider the spatial relationships and interactions between adjacent pixels. In contrast, methods from computer vision analysis exploit the interdependence between different pixels.

Our method, *Latent Unmixing*, is a novel approach for processing mixed images into their individual contributing components that borrows from computer vision to solve the signal processing problem in experimental physics use cases. It relies on a three-dimensional Convolutional Neural Network (3D CNN) to capture and combine features from different dimensions simultaneously, leading to improved representations of complex patterns in the three-dimensional space [Wang et al. 2023]. Deep learning methods have previously been proposed for the task of unmixing volumetric data, especially for hyperspectral measurements [Ghosh et al. 2022, Bhatt et al. 2020, Wang et al. 2019]. For remote sensing applications, the deep learning models for processing hyperspectral data – either for classification [Ahmad et al. 2020, Yang et al. 2020, Jung et al. 2022], super-resolution [Ma et al. 2023], denoising [Shi et al. 2021], or unmixing [Tao et al. 2022, Qi et al. 2020] – are generally based on 3D CNNs to process the raw hyperspectral measurements as volumetric data. *Latent Unmixing* uses a 3D U-Net to combine the spatial and time/spectral dimensions in contexts where, if taken individually, each dimension (spatial and time/spectral) does not include enough information to allow correct separation of the components. By integrating these spatial relationships, more information is extracted, achieving more accurate unmixing results. Our approach takes advantage of an already demonstrated neural network architecture, the 3D U-Net, but the architecture choice is not a limiting factor of the method: it could easily be adapted to other architectures. Other works previously used the disentangled representation of input data in the latent space of an autoencoder to unmix hyperspectral data [Sahoo et al. 2022, Palsson et al. 2018]. In

contrast to the *Latent Unmixing* method, they either require precise reference spectra [Sahoo et al. 2022, Borsoi et al. 2023], or do not account for the shared information between neighboring pixels [Palsson et al. 2018].

Our approach is first illustrated and validated on a toy synthetic dataset based on MNIST, where digit images are juxtaposed, generating the time dimension with different configurations for each of the class used. This toy dataset confirmed the validity of the *Latent Unmixing* method by demonstrating its superiority over a pixel-wise curve fitting method (MLE, Appendix D) and a spatial-only method (2D U-Net, Appendix C). We then demonstrated the *Latent Unmixing* method for two experimental contexts: FLIM and mode decomposition in optical fibers, exemplifying the generalizability of the method to different signal distributions and experimental settings. In both cases, our method adapts to class unbalance across data samples (number of photons per pixel in FLIM and number of propagating modes in MMF). In this study, we crafted datasets that accurately represent real experiments, while providing an associated ground truth to evaluate the performance of the proposed latent unmixing approach. Our dataset format can easily be adapted to fit specific parameters, distributions, number of channels, and ranges of lifetime or wavelength values. Even though the *Latent Unmixing* method was trained with a time dimension completely simulated from sampling in exponential decay functions, the results on real FLIM measurements support that the method can be applied to real measurements.

In conclusion, the *Latent Unmixing* method takes advantage of the capacity of deep multidimensional convolutional neural networks to combine the information from all dimensions, which allows unmixing undersampled and noisy data. This work was concentrated on 3D measurements, but future work could explore the potential of multi-dimensional CNNs for *Latent Unmixing* over higher numbers of dimensions, e.g. spectral-FLIM microscopy [Chen et al. 2021] (x, y, λ, τ). Our method was crafted in a way that is generalizable to different numbers of target channels (1-4 for 3D-MNIST, 2-4 for FLIM-STED, 1-6 for S²-MMF) and different types of distributions (exponential decay curves, interfering sinusoidal signals). This novel use of deep neural networks showcases the capacity of deep networks to process sparse information in its entirety, which is of great interest for a range of imaging applications.

Acknowledgements. Albert Michaud-Gagnon and Marie Lafontaine for the implementation of the 2-species phasors unmixing method.

Declarations

4.1 Funding

Funding was provided by grants from the Natural Sciences and Engineering Research Council of Canada (NSERC) (RGPIN-06704-2019 to F.L.C. and RGPIN-2019-06706 to C.G.), Fonds de Recherche Nature et Technologie (FRQNT) Team Grant (2021-PR-284335 to F.L.C. and C.G.), the Canadian Institute for Health Research (CIHR) (202109PJT-471107-NSB-CFBA-12805 to F.L.C.), the Sentinel North Initiative (F.L.C. and C.G.), and the Neuronex Initiative (National Science Foundation 2014862, Fond de recherche du Québec - Santé 295824) (F.L.C.). C.G. is a CIFAR

Canada AI Chair and F.L.C. is a Canada Research Chair Tier II. C.B. is supported by scholarships from NSERC, from the Fonds de Recherche Nature et Technologie (FRQNT) Quebec, from the FRQNT strategic cluster UNIQUE, and by a Leadership and Scientific Engagement Award from Université Laval. V.B. is supported by a scholarship from NSERC.

4.2 Competing interests

The authors have no competing interests to declare that are relevant to the content of this article.

4.3 Code availability

All scripts used to generate the 3D-MNIST dataset and the time dimension of the FLIM-STED dataset, train the models, test the models with trained weights, and produce the results presented here is available to download at <https://github.com/FLClab/LatentUnmixing>. All experiments were conducted using Python 3.8.10, with the library versions indicated in the Github repository.

4.4 Data availability

All datasets are available to download at <https://s3.valeria.science/flclab-unmixing/index.html>.

4.5 Authors contribution

C.B., F.L.C. and C.G. have conceptualized the method. C.B. has implemented the method and ran the experiments. A.D. has implemented the phasor analysis method and acquired the real FLIM images. V.B. has generated the simulated S^2 data and analyzed the results. J-M.B., J.C. and A.P.R. have acquired the 4-colors confocal and STED images used for training and testing. C.B., A.D., V.B., C.G. and F.L.C. have written the manuscript.

References

- [Ahmad et al. 2020] Ahmad, M., Khan, A.M., Mazzara, M., Distefano, S., Ali, M., Sarfraz, M.S.: A fast and compact 3-d cnn for hyperspectral image classification. *IEEE Geoscience and Remote Sensing Letters* **19**, 1–5 (2020)
- [Ahmed-Cox et al. 2022] Ahmed-Cox, A., Macmillan, A.M., Pandzic, E., Whan, R.M., Kavallaris, M.: Application of rapid fluorescence lifetime imaging microscopy (rapidflim) to examine dynamics of nanoparticle uptake in live cells. *Cells* **11**(4), 642 (2022)
- [An et al. 2020] An, Y., Huang, L., Li, J., Leng, J., Yang, L., Zhou, P.: Deep learning-based real-time mode decomposition for multimode fibers. *IEEE Journal of Selected Topics in Quantum Electronics* **26**(4), 1–6 (2020). <https://doi.org/10.1109/JSTQE.2020.2969511>
- [Andronov et al. 2022] Andronov, L., Genthial, R., Hentsch, D. & Klaholz, B. P. (2022). splitSMLM, a spectral demixing method for high-precision multi-color localization microscopy applied to nuclear pore complexes. *Communications Biology*, *5*(1), 1100.
- [Bajzer et al. 1991] Bajzer, Ž., Therneau, T.M., Sharp, J.C., Prendergast, F.G.: Maximum likelihood method for the analysis of time-resolved fluorescence decay curves. *European biophysics journal* **20**, 247–262 (1991)
- [Barroso et al. 2023] Barroso, M., Monaghan, M.G., Niesner, R., Dmitriev, R.I.: Probing organoid metabolism using fluorescence lifetime imaging microscopy (flim): The next frontier of drug discovery and disease understanding. *Advanced Drug Delivery Reviews* p. 115081 (2023)
- [Beaupré et al. 2024] Beaupré, F., Bilodeau, A., Wiesner, T., Leclerc, G., Lemieux, M., Nadeau, G., ... & Lavoie-Cardinal, F. (2024). Quantitative Analysis of Miniature Synaptic Calcium Transients Using Positive Unlabeled Deep Learning. *bioRxiv*, 2024-07.
- [Becker et al. 2012] Becker, W.: Fluorescence lifetime imaging—techniques and applications. *Journal of microscopy* **247**(2), 119–136 (2012)
- [Berezin et al. 2010] Berezin, M.Y., Achilefu, S.: Fluorescence lifetime measurements and biological imaging. *Chemical reviews* **110**(5), 2641–2684 (2010)
- [Bhatt et al. 2020] Bhatt, J.S., Joshi, M.V.: Deep learning in hyperspectral unmixing: A review. In: *IGARSS 2020-2020 IEEE International Geoscience and Remote Sensing Symposium*. pp. 2189–2192. IEEE (2020)
- [Bories et al. 2012] Bories, C., Guitton, M. J., Julien, C., Tremblay, C., Vandal, M., Msaid, M., ... & Calon, F. (2012). Sex-dependent alterations in social behaviour and cortical synaptic activity coincide at different ages in a model of Alzheimer’s disease.
- [Borsoi et al. 2023] Borsoi, R.A., Erdo, D., Imbiriba, T., et al.: Learning interpretable deep disentangled neural networks for hyperspectral unmixing. *IEEE Transactions on Computational Imaging* (2023)
- [Bucker et al. 2011] Bückers, J., Wildanger, D., Vicidomini, G., Kastrup, L., & Hell, S. W. (2011). Simultaneous multi-lifetime multi-color STED imaging for colocalization analyses. *Optics express*, *19*(4), 3130-3143.

- [Byrd et al. 1995] Byrd, R. H., Lu, P., Nocedal, J., & Zhu, C. (1995). A limited memory algorithm for bound constrained optimization. *SIAM Journal on scientific computing*, 16(5), 1190-1208.
- [Chen et al. 2021] Chen, K., Yan, R., Xiang, L., & Xu, K. (2021). Excitation spectral microscopy for highly multiplexed fluorescence imaging and quantitative biosensing. *Light: Science & Applications*, 10(1), 97.
- [Chen et al. 2022] Chen, Y.I., Chang, Y.J., Liao, S.C., Nguyen, T.D., Yang, J., Kuo, Y.A., Hong, S., Liu, Y.L., Rylander III, H.G., Santacruz, S.R., et al.: Generative adversarial network enables rapid and robust fluorescence lifetime image analysis in live cells. *Communications Biology* 5(1), 18 (2022)
- [Chen et al. 2023] Chen, P., Kang, Q., Niu, J., Jing, Y., Zhang, X., Yu, B., Qu, J., Lin, D.: Fluorescence lifetime tracking and imaging of single moving particles assisted by a low-photon-count analysis algorithm. *Biomedical Optics Express* 14(4), 1718 (Apr 2023)
- [Chen et al. 2023] Chen, Y. I., Chang, Y. J., Sun, Y., Liao, S. C., Santacruz, S. R., & Yeh, H. C. (2023). Spatial resolution enhancement in photon-starved STED imaging using deep learning-based fluorescence lifetime analysis. *Nanoscale*, 15(21), 9449-9456.
- [Chessel et al. 2013] Chessel, A., Waharte, F., Salamero, J., Kervrann, C.: A maximum likelihood method for lifetime estimation in photon counting-based fluorescence lifetime imaging microscopy. In: 21st European Signal Processing Conference (EUSIPCO 2013). pp. 1–5. IEEE (2013)
- [Çiçek et al. 2016] Çiçek, Ö., Abdulkadir, A., Lienkamp, S. S., Brox, T., & Ronneberger, O. (2016). 3D U-Net: learning dense volumetric segmentation from sparse annotation. In *Medical Image Computing and Computer-Assisted Intervention—MICCAI 2016: 19th International Conference, Athens, Greece, October 17-21, 2016, Proceedings, Part II* 19 (pp. 424-432). Springer International Publishing.
- [Dani et al. 2010] Dani, A., Huang, B., Bergan, J., Dulac, C., & Zhuang, X. (2010). Superresolution imaging of chemical synapses in the brain. *Neuron*, 68(5), 843-856.
- [Digman et al. 2008] Digman, M.A., Caiolfa, V.R., Zamai, M., Gratton, E.: The phasor approach to fluorescence lifetime imaging analysis. *Biophysical journal* 94(2), L14–L16 (2008)
- [Dong et al. 2003] Dong, C. Y., French, T., So, P. T., Buehler, C., Berland, K. M., & Gratton, E. (2003). Fluorescence-lifetime imaging techniques for microscopy. *Methods in cell biology*, 72, 431-464.
- [Dong et al. 2020] Dong, L., Yuan, Y., Luxs, X.: Spectral–spatial joint sparse nmf for hyperspectral unmixing. *IEEE Transactions on Geoscience and Remote Sensing* 59(3), 2391–2402 (2020)
- [Enderlein et al. 1997] Enderlein, J., Goodwin, P. M., Van Orden, A., Ambrose, W. P., Erdmann, R., & Keller, R. A. (1997). A maximum likelihood estimator to distinguish single molecules by their fluorescence decays. *Chemical physics letters*, 270(5-6), 464-470.
- [Enderlein et al. 2001] Enderlein, J., & Sauer, M. (2001). Optimal algorithm for

- single-molecule identification with time-correlated single-photon counting. *The Journal of Physical Chemistry A*, 105(1), 48-53.
- [Falk et al. 2019] Falk, T., Mai, D., Bensch, R., Çiçek, Ö., Abdulkadir, A., Marrakchi, Y., ... & Ronneberger, O. (2019). U-Net: deep learning for cell counting, detection, and morphometry. *Nature methods*, 16(1), 67-70.
- [Fallahkhair et al. 2008] Fallahkhair, A., Li, K.S., Murphy, T.E.: Vector finite difference modesolver for anisotropic dielectric waveguides. *J. Lightwave Technol.* **26**(11), 1423–1431 (Jun 2008), <https://opg.optica.org/jlt/abstract.cfm?URI=jlt-26-11-1423>
- [Fang et al. 2020] Fang, B., Bai, Y., & Li, Y. (2020). Combining spectral unmixing and 3d/2d dense networks with early-exiting strategy for hyperspectral image classification. *Remote Sensing*, 12(5), 779.
- [Frei et al. 2022] Frei, M. S., Koch, B., Hiblot, J., & Johnsson, K. (2022). Live-cell fluorescence lifetime multiplexing using synthetic fluorescent probes. *ACS Chemical Biology*, 17(6), 1321-1327.
- [Frei et al. 2022] Frei, M.S., Tarnawski, M., Roberti, M.J., Koch, B., Hiblot, J., Johnsson, K.: Engineered halotag variants for fluorescence lifetime multiplexing. *Nature methods* **19**(1), 65–70 (2022)
- [Ghosh et al. 2022] Ghosh, P., Roy, S. K., Koirala, B., Rasti, B., & Scheunders, P. (2022). Hyperspectral unmixing using transformer network. *IEEE Transactions on Geoscience and Remote Sensing*, **60**, 1-16.
- [Gloge et al. 1972] Gloge, D.: Optical power flow in multimode fibers. *Bell System Technical Journal* **51**(8), 1767–1783 (1972)
- [Gonzalez et al. 2022] Gonzalez Pisfil, M., Nadelson, I., Bergner, B., Rottmeier, S., Thomae, A. W., & Dietzel, S. (2022). Stimulated emission depletion microscopy with a single depletion laser using five fluorochromes and fluorescence lifetime phasor separation. *Scientific Reports*, 12(1), 14027.
- [Goodfellow et al. 2016] Goodfellow, I., Bengio, Y., Courville, A., & Bengio, Y. (2016). *Deep Learning*. MIT Press.
- [Heinz et al. 2001] Heinz, D.C., et al.: Fully constrained least squares linear spectral mixture analysis method for material quantification in hyperspectral imagery. *IEEE transactions on geoscience and remote sensing* **39**(3), 529–545 (2001)
- [Ho et al. 2020] Ho, J., Jain, A., & Abbeel, P. (2020). Denoising diffusion probabilistic models. *Advances in neural information processing systems*, **33**, 6840-6851.
- [Huang et al. 2015] Huang, L., Guo, S., Leng, J., Lü, H., Zhou, P., Cheng, X.: Real-time mode decomposition for few-mode fiber based on numerical method. *Opt. Express* **23**(4), 4620–4629 (2015). <https://doi.org/10.1364/OE.23.004620>, <https://opg.optica.org/oe/abstract.cfm?URI=oe-23-4-4620>
- [Iordache et al. 2011] Iordache, M. D., Bioucas-Dias, J. M., & Plaza, A. (2011). Sparse unmixing of hyperspectral data. *IEEE Transactions on Geoscience and Remote Sensing*, 49(6), 2014-2039.
- [Ji et al. 2012] Ji, S., Xu, W., Yang, M., Yu, K.: 3d convolutional neural networks for human action recognition. *IEEE transactions on pattern analysis and machine intelligence* **35**(1), 221–231 (2012)
- [Jung et al. 2022] Jung, D.H., Kim, J.D., Kim, H.Y., Lee, T.S., Kim, H.S., Park, S.H.:

- A hyperspectral data 3d convolutional neural network classification model for diagnosis of gray mold disease in strawberry leaves. *Frontiers in Plant Science* **13**, 837020 (2022)
- [Keshava et al. 2002] Keshava, N., & Mustard, J. F. (2002). Spectral unmixing. *IEEE signal processing magazine*, *19*(1), 44-57.
- [Lagache et al. 2018] Lagache, T., Grassart, A., Dallongeville, S., Faklaris, O., Sauvonnnet, N., Dufour, A., ... & Olivo-Marin, J. C. (2018). Mapping molecular assemblies with fluorescence microscopy and object-based spatial statistics. *Nature communications*, *9*(1), 698.
- [Lecun et al. 1998] LeCun, Y., Bottou, L., Bengio, Y., Haffner, P.: Gradient-based learning applied to document recognition. *Proceedings of the IEEE* **86**(11), 2278–2324 (1998).
- [Levitt et al. 2020] Levitt, J. A., Poland, S. P., Krstajic, N., Pfisterer, K., Erdogan, A., Barber, P. R., ... & Ameer-Beg, S. M. (2020). Quantitative real-time imaging of intracellular FRET biosensor dynamics using rapid multi-beam confocal FLIM. *Scientific Reports*, *10*(1), 5146.
- [Liao et al. 2014] Liao, S.C., Sun, Y., Coskun, U.: Flim analysis using the phasor plots. ISS Inc.: Champaign, IL, USA **61822** (2014)
- [Lin et al. 2015] Lin, C. H., Chi, C. Y., Wang, Y. H., & Chan, T. H. (2015). A fast hyperplane-based minimum-volume enclosing simplex algorithm for blind hyperspectral unmixing. *IEEE Transactions on Signal Processing*, *64*(8), 1946-1961.
- [Liu et al. 2019] Liu, Y., Jun, E., Li, Q., Heer, J. (2019). Latent space cartography: Visual analysis of vector space embeddings. *Computer graphics forum* **38**(3)
- [Ma et al. 2023] Ma, Q., Jiang, J., Liu, X., Ma, J.: Learning a 3d-cnn and transformer prior for hyperspectral image super-resolution. *Information Fusion* **100**, 101907 (2023)
- [Mannam et al. 2020] Mannam, V., Zhang, Y., Yuan, X., Ravasio, C., & Howard, S. S. (2020). Machine learning for faster and smarter fluorescence lifetime imaging microscopy. *Journal of Physics: Photonics*, *2*(4), 042005.
- [Manuylovich et al. 2020] Manuylovich, E.S., Dvoyrin, V.V., Turitsyn, S.K.: Fast mode decomposition in few-mode fibers. *Nature Communications* **11**(5507) (2020). <https://doi.org/10.1038/s41467-020-19323-6>
- [Maus et al. 2001] Maus, M., Cotlet, M., Hofkens, J., Gensch, T., De Schryver, F. C., Schaffer, J., & Seidel, C. A. M. (2001). An experimental comparison of the maximum likelihood estimation and nonlinear least-squares fluorescence lifetime analysis of single molecules. *Analytical chemistry*, **73**(9), 2078-2086.
- [McRae et al. 2019] McRae, T. D., Oleksyn, D., Miller, J., & Gao, Y. R. (2019). Robust blind spectral unmixing for fluorescence microscopy using unsupervised learning. *Plos one*, *14*(12), e0225410.
- [Montag et al. 2016] Montag, M. J., & Stephani, H. (2016). Hyperspectral unmixing from incomplete and noisy data. *Journal of Imaging*, *2*(1), 7.
- [Mustard et al. 1987] Mustard, J. F., & Pieters, C. M. (1987). Quantitative abundance estimates from bidirectional reflectance measurements. *Journal of Geophysical Research: Solid Earth*, *92*(B4), E617-E626.

- [Nasser et al. 2022] Nasser, M., Meller, A.: Lifetime-based analysis of binary fluorophores mixtures in the low photon count limit. *Iscience* **25**(1) (2022)
- [Nault et al. 2010] Nault, F., & De Koninck, P. (2010). Dissociated hippocampal cultures. *Protocols for Neural Cell Culture: Fourth Edition*, 137-159.
- [Nguyen et al. 2012] Nguyen, D.M., Blin, S., Nguyen, T.N., Le, S.D., Provino, L., Thual, M., Chartier, T.: Modal decomposition technique for multimode fibers. *Appl. Opt.* **51**(4), 450–456 (2012). <https://doi.org/10.1364/AO.51.000450>, <https://opg.optica.org/ao/abstract.cfm?URI=ao-51-4-450>
- [Nicholson et al. 2008] Nicholson, J., Yablon, A.D., Ramachandran, S., Ghalmi, S.: Spatially and spectrally resolved imaging of modal content in large-mode-area fibers. *Optics express* **16**(10), 7233–7243 (2008)
- [Nicole et al. 2018] Nicole, O., Bell, D. M., Leste-Lasserre, T., Doat, H., Guillemot, F., & Pacary, E. (2018). A novel role for CAMKII β in the regulation of cortical neuron migration: implications for neurodevelopmental disorders. *Molecular psychiatry*, **23**(11), 2209-2226.
- [Palsson et al. 2018] Palsson, B., Sigurdsson, J., Sveinsson, J.R., Ulfarsson, M.O.: Hyperspectral unmixing using a neural network autoencoder. *IEEE Access* **6**, 25646–25656 (2018)
- [Peter et al. 2005] Peter, M., Ameer-Beg, S. M., Hughes, M. K., Keppler, M. D., Prag, S., Marsh, M., ... & Ng, T. (2005). Multiphoton-FLIM quantification of the EGFP-mRFP1 FRET pair for localization of membrane receptor-kinase interactions. *Biophysical journal*, **88**(2), 1224-1237.
- [Qi et al. 2020] Qi, L., Li, J., Wang, Y., Lei, M., Gao, X.: Deep spectral convolution network for hyperspectral image unmixing with spectral library. *Signal Processing* **176**, 107672 (2020)
- [Quiquempois et al. 2021] Quiquempois, Y., Sévigny, B., Andresen, E.R., Chedid, A., Bigot, L.: Mode recovery by S2 imaging without a fourier transform. *J. Light-wave Technol.* **39**(13), 4453–4461 (2021), <https://opg.optica.org/jlt/abstract.cfm?URI=jlt-39-13-4453>
- [Rahim et al. 2022] Rahim, M. K., Zhao, J., Patel, H. V., Lagouros, H. A., Kota, R., Fernandez, I., ... & Haun, J. B. (2022). Phasor analysis of fluorescence lifetime enables quantitative multiplexed molecular imaging of three probes. *Analytical chemistry*, **94**(41), 14185-14194.
- [Ranjit et al. 2018] Ranjit, S., Malacrida, L., Jameson, D.M., Gratton, E.: Fit-free analysis of fluorescence lifetime imaging data using the phasor approach. *Nature protocols* **13**(9), 1979–2004 (2018)
- [Ronneberger et al. 2015] Ronneberger, O., Fischer, P., & Brox, T. (2015). U-net: Convolutional networks for biomedical image segmentation. In *Medical image computing and computer-assisted intervention—MICCAI 2015: 18th international conference, Munich, Germany, October 5-9, 2015, proceedings, part III 18* (pp. 234-241). Springer International Publishing.
- [Rowley et al. 2011] Rowley, M.I., Barber, P.R., Coolen, A.C.C., Vojnovic, B.: Bayesian analysis of fluorescence lifetime imaging data. In: Periasamy, A., König, K., So, P.T.C. (eds.) *SPIE BiOS*. p. 790325. San Francisco, California, USA (2011)

- [Sahoo et al. 2022] Sahoo, M.M., Porwal, A., Karnieli, A., et al.: Deep-learning-based latent space encoding for spectral unmixing of geological materials. *ISPRS Journal of Photogrammetry and Remote Sensing* **183**, 307–320 (2022)
- [Sevigny et al. 2014] Sévigny, B., Le Cocq, G., Carrero, C.C.C., Valentin, C., Sillard, P., Bouwmans, G., Bigot, L., Quiquempois, Y.: Advanced s^2 imaging: Application of multivariate statistical analysis to spatially and spectrally resolved datasets. *Journal of Lightwave Technology* **32**(23), 4606–4612 (2014). <https://doi.org/10.1109/JLT.2014.2362960>
- [Sewell et al. 2015] Sewell, D., Kim, H., Ha, T., & Ma, P. (2015). A parameter estimation method for fluorescence lifetime data. *BMC research notes*, 8, 1-9.
- [Shannon 1949] Shannon, C. E. (1949). Communication in the Presence of Noise. *Proceedings of the IRE*, 37(1), 10–21.
- [Shi et al. 2021] Shi, Q., Tang, X., Yang, T., Liu, R., Zhang, L.: Hyperspectral image denoising using a 3-d attention denoising network. *IEEE Transactions on Geoscience and Remote Sensing* **59**(12), 10348–10363 (2021)
- [Shimabukuro et al. 1991] Shimabukuro, Y.E., Smith, J.A.: The least-squares mixing models to generate fraction images derived from remote sensing multispectral data. *IEEE Transactions on Geoscience and Remote sensing* **29**(1), 16–20 (1991)
- [Smith et al. 2019] Smith, J.T., Yao, R., Sinsuebphon, N., Rudkouskaya, A., Un, N., Mazurkiewicz, J., Barroso, M., Yan, P., Intes, X.: Fast fit-free analysis of fluorescence lifetime imaging via deep learning. *Proceedings of the National Academy of Sciences* **116**(48), 24019–24030 (2019)
- [Smith et al. 2020] Smith, J.T., Ochoa, M., Intes, X.: Unmix-me: spectral and lifetime fluorescence unmixing via deep learning. *Biomedical Optics Express* **11**(7), 3857–3874 (2020)
- [Stringari et al. 2011] Stringari, C., Cinquin, A., Cinquin, O., Digman, M. A., Donovan, P. J., & Gratton, E. (2011). Phasor approach to fluorescence lifetime microscopy distinguishes different metabolic states of germ cells in a live tissue. *Proceedings of the national academy of sciences*, **108**(33), 13582-13587
- [Sun et al. 2017] Sun, Y., Tortarolo, G., Teng, K. W., Ishitsuka, Y., Coskun, U. C., Liao, S. C. J., ... & Barbieri, B. (2017). A novel pulsed STED microscopy method using FastFLIM and the phasor plots. In *Multiphoton Microscopy in the Biomedical Sciences XVII* (Vol. 10069, pp. 136-151). SPIE.
- [Sun et al. 2024] Sun, Y., Tortarolo, G., Chen, Y. I., Chang, Y. J., Coskun, U. C., Liao, S. C. J., ... & Yeh, H. C. (2024). Enhancing the resolution of STED microscopy by SPLIT and flimGANE. In *Multiphoton Microscopy in the Biomedical Sciences XXIV* (Vol. 12847, pp. 17-31). SPIE.
- [Szmactinski et al. 1995] Szmactinski, H., Lakowicz, J.R.: Fluorescence lifetime-based sensing and imaging. *Sensors and Actuators B: Chemical* **29**(1-3), 16–24 (1995)
- [Tadokoro et al. 2023] Tadokoro, R., Yamada, R., Kataoka, H.: Pre-training auto-generated volumetric shapes for 3d medical image segmentation. In: *Proceedings of the IEEE/CVF Conference on Computer Vision and Pattern Recognition*. pp. 4739–4744 (2023)
- [Tang et al. 2016] Tang, A. H., Chen, H., Li, T. P., Metzbowler, S. R., MacGillavry,

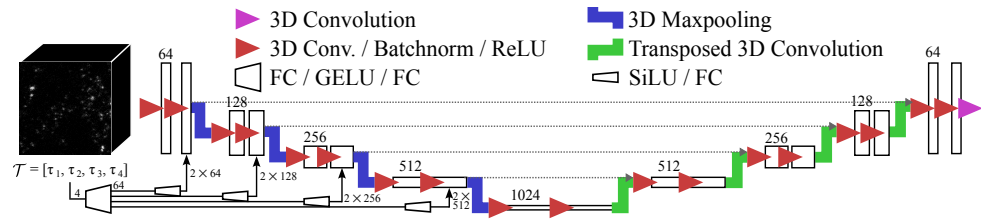
- H. D., & Blanpied, T. A. (2016). A trans-synaptic nanocolumn aligns neurotransmitter release to receptors. *Nature*, *536*(7615), 210-214.
- [Tang et al. 2019] Tang, S., Xu, Y., Huang, L., Sun, L.: Hyperspectral image super-resolution via adaptive dictionary learning and double l1 constraint. *Remote Sensing* **11**(23), 2809 (2019)
- [Tao et al. 2022] Tao, X., Paoletti, M., Han, L., Wu, Z., Jiménez, L., Haut, J., Ren, P., Plaza, J., Plaza, A.: A new 3d convolution network for hyperspectral unmixing. In: *IGARSS 2022-2022 IEEE International Geoscience and Remote Sensing Symposium*. pp. 1620–1623. IEEE (2022)
- [Tardif et al. 2019] Tardif, C., Nadeau, G., Labrecque, S., Côté, D., Lavoie-Cardinal, F., & De Koninck, P. (2019). Fluorescence lifetime imaging nanoscopy for measuring Förster resonance energy transfer in cellular nanodomains. *Neurophotonics*, *6*(1), 015002-015002.
- [Tortarolo et al. 2019] Tortarolo, G., Sun, Y., Shah, S., Barbieri, B., Teng, K. W., Ishitsuka, Y., ... & Vicidomini, G. (2019). The SPLIT approach for enhancing the spatial resolution in pulsed STED microscopy with FastFLIM and phasor plots. In *Multiphoton Microscopy in the Biomedical Sciences XIX* (Vol. 10882, pp. 59-69). SPIE.
- [Turton et al. 2003] Turton, D. A., Reid, G. D., & Beddard, G. S. (2003). Accurate analysis of fluorescence decays from single molecules in photon counting experiments. *Analytical chemistry*, *75*(16), 4182-4187.
- [Vallmitjana et al. 2022] Vallmitjana, A., Lepanto, P., Irigoien, F., & Malacrida, L. (2022). Phasor-based multi-harmonic unmixing for in-vivo hyperspectral imaging. *Methods and Applications in Fluorescence*, *11*(1), 014001.
- [Valm et al. 2017] Valm, A.M., Cohen, S., Legant, W.R., Melunis, J., Hershberg, U., Wait, E., Cohen, A.R., Davidson, M.W., Betzig, E., Lippincott-Schwartz, J.: Applying systems-level spectral imaging and analysis to reveal the organelle interactome. *Nature* **546**(7656), 162–167 (2017)
- [Wang et al. 2016] Wang, W., Qian, Y., Tang, Y.Y.: Hypergraph-regularized sparse nmf for hyperspectral unmixing. *IEEE journal of selected topics in applied earth observations and remote sensing* **9**(2), 681–694 (2016)
- [Wang et al. 2019] Wang, C.J., Li, H., Tang, Y.Y.: Hyperspectral unmixing using deep learning. In: *2019 International Conference on Wavelet Analysis and Pattern Recognition (ICWAPR)*. pp. 1–7. IEEE (2019)
- [Wang et al. 2023] Wang, C.: A review on 3d convolutional neural network. In: *2023 IEEE 3rd International Conference on Power, Electronics and Computer Applications (ICPECA)*. pp. 1204–1208 (2023). <https://doi.org/10.1109/ICPECA56706.2023.10075760>
- [Weigert et al. 2018] Weigert, M., Schmidt, U., Boothe, T., Müller, A., Dibrov, A., Jain, A., ... & Myers, E. W. (2018). Content-aware image restoration: pushing the limits of fluorescence microscopy. *Nature methods*, *15*(12), 1090-1097.
- [Wiesner et al. 2020] Wiesner, T., Bilodeau, A., Bernatchez, R., Deschênes, A., Raulier, B., De Koninck, P., & Lavoie-Cardinal, F. (2020). Activity-dependent remodeling of synaptic protein organization revealed by high throughput analysis of STED nanoscopy images. *Frontiers in neural circuits*, *14*, 57.

- [Yang et al. 2020] Yang, Q., Liu, Y., Zhou, T., Peng, Y., Tang, Y.: 3d convolutional neural network for hyperspectral image classification using generative adversarial network. In: 2020 13th International Conference on Intelligent Computation Technology and Automation (ICICTA). pp. 277–283. IEEE (2020)
- [Zack et al. 1977] Zack, G. W., Rogers, W. E., & Latt, S. A. (1977). Automatic measurement of sister chromatid exchange frequency. *Journal of Histochemistry & Cytochemistry*, 25(7), 741-753.
- [Zang et al. 2023] Zang, Z., Xiao, D., Wang, Q., Jiao, Z., Chen, Y., Li, D.D.U.: Compact and robust deep learning architecture for fluorescence lifetime imaging and FPGA implementation. *Methods and Applications in Fluorescence* 11(2), 025002 (2023)
- [Zhang et al. 2016] Zhang, Y., Cuyt, A., Lee, W. S., Bianco, G. L., Wu, G., Chen, Y., & Li, D. D. U. (2016). Towards unsupervised fluorescence lifetime imaging using low dimensional variable projection. *Optics Express*, 24(23), 26777-26791.

Appendices

Appendix A: Architecture and training parameters

Suppl. table 1 summarizes the architecture parameters for the 3D U-Net (Suppl. fig. 1) used to obtain the results presented in this paper. All kernel sizes used throughout the network are $3 \times 3 \times 3$, and convolutions use zero-padding of size 1 along the three dimensions. Suppl. table 2 describes the layers inside the DoubleConv3D blocks. For the experiments performed in this study, the receptive field of the final layer spans 110 pixels in width, height, and depth, contrasting with pixelwise approaches for which the predictive capacity is restricted by the very limited information of a single pixel or a narrow and fixed neighbourhood.



Supplementary Figure 1 The 3D U-Net network architecture used for unmixing the FLIM-STED dataset. For 3D-MNIST and S²-MMF, the conditioning branch with the encoder and layer-specific fully-connected layers is not used. A smaller version is used for S²-MMF, with 3 Down and Up blocks instead of 4.

Down3D blocks are a MaxPooling layer with kernels of shape $2 \times 2 \times 2$ and a stride of 2, followed by a DoubleConv3D block. Up3D blocks are DoubleConv3D blocks preceded by a 3D transposed convolution, also with kernels of shape $2 \times 2 \times 2$ and a stride of 2. The last convolution, OutConv3D, is a simple convolution with kernels of size $1 \times 1 \times 1$ and a stride of 1, to remove a dimension before applying the bandpass filters.

Suppl. table 3 summarizes the training hyper-parameters used for each dataset.

Block	Type	In Ch.	Out Ch.
1	DoubleConv3D	L	64
2	Down3D	64	128
3	Down3D	128	256
4	Down3D	256	512
5	Down3D	512	1024
6	Up3D	1024	512
7	Up3D	512	256
8	Up3D	256	128
9	Up3D	128	64
10	OutConv3D	64	1

Supplementary Table 1 Architecture of the 3D-UNet used to produce the results presented in this paper. Dimension L is 28 for 3D-MNIST, 40 for FLIM-STED, and 60 for S²-MMF. Blocks 5 and 6 were removed for S²-MMF.

Layer	Type	Channels
1	Convolution	In Ch. \rightarrow Out ch.
2	BatchNorm3d	Out Ch. \rightarrow Out ch.
3	ReLU	
4	Convolution	Out Ch. \rightarrow Out ch.
5	BatchNorm3d	Out Ch. \rightarrow Out ch.
6	ReLU	

Supplementary Table 2 Layers of the DoubleConv3D block.

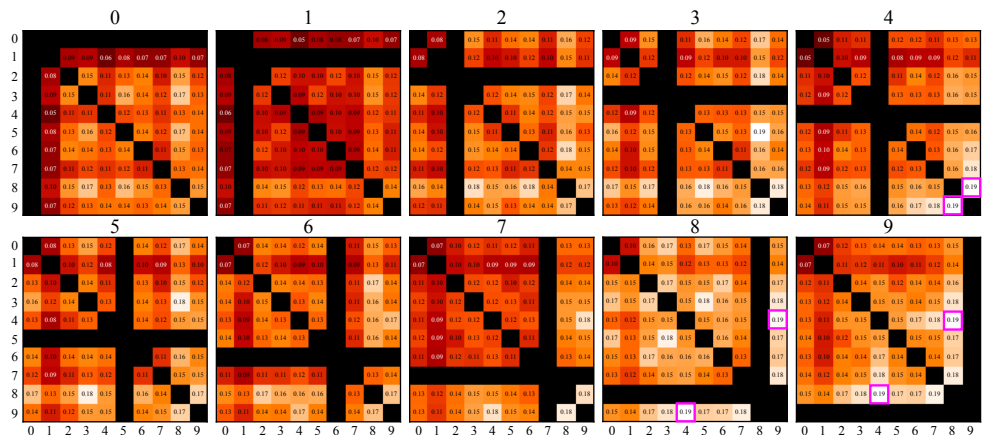
Hyperparameter	3D-MNIST	FLIM-STED	S ² -MMF
Learning rate	0.01	0.01	0.01
Batch size	64	12	16
Input size	$28^2 \times 28$	$96^2 \times 40$	$64^2 \times 60$
Output size	$28^2 \times 28$	$96^2 \times 40$	$64^2 \times 60$
# Filters	4	5	6
Filter width	7	8	10
# images	8,000	1,132	1,500
Best epoch	167	272	182

Supplementary Table 3 Training hyperparameters used to obtain the results presented in this paper. Best epoch is the epoch where the validation loss reaches a minimum.

Appendix B: Generation of the 3D-MNIST dataset

The 3D-MNIST dataset was created by combining images of up to 3 digits from the original MNIST dataset [Lecun et al. 1998]. To increase the complexity of the unmixing process, we deliberately selected three digits characterized by the highest degree of overlap, ensuring that a substantial number of pixels would count multiple components. To find the trio of digits with the highest fraction of overlap, 1000 samples of each combination of three digits were randomly sampled in the MNIST training set and the average intersection over union was computed. The IOU for all triplets

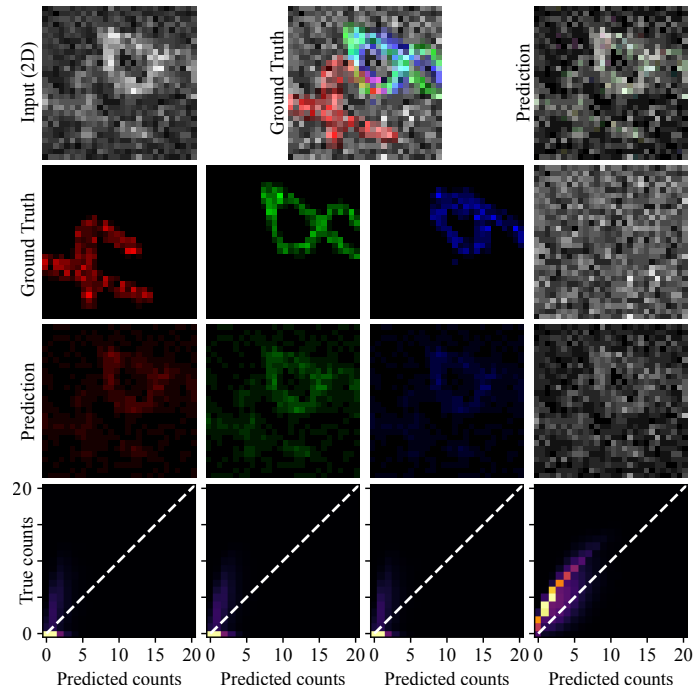
are shown in Suppl. Fig. 2. The maximum average IOU (0.19) is obtained from the combination of digits 4, 8 and 9.



Supplementary Figure 2 Intersection over union between all digits of MNIST (from top-left to bottom-right: 0, 1, ... 9). Diagonals are left blank to avoid identical pairs of digits. Digits 4, 8, and 9 (highlighted in magenta) have the highest average intersection over union (0.19), making it the most difficult trio of digits to separate.

Appendix C. 2D U-Net for unmixing MNIST

To evaluate how the time dimension is exploited by the network to solve the unmixing task, a 2D version of the 3D-MNIST dataset was generated by omitting lines 23-26 and 30-33 in algorithm 2; that is, by simply not creating the time dimension after creating the noisy overlapping digits. Results obtained by applying a 2D U-Net on this 2D-dataset are shown in Suppl. Fig. 3. The 2D U-Net can not separate the digits through the noise, demonstrating that the third dimension is useful for unmixing the overlapping digits.

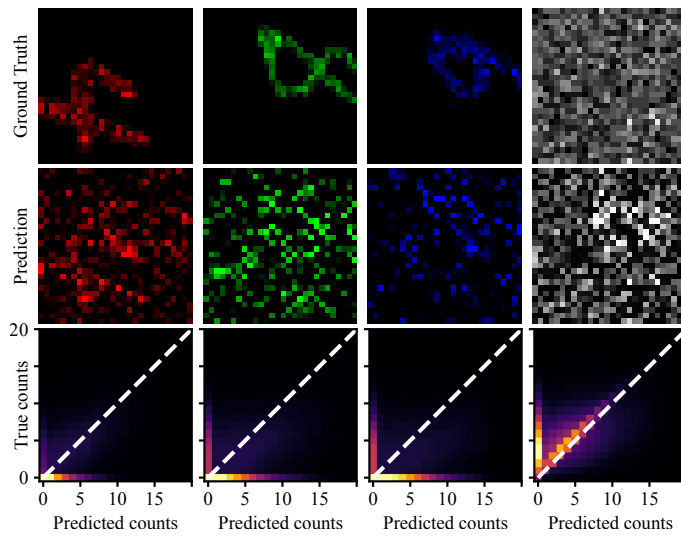


Supplementary Figure 3 Example result obtained with a 2D U-Net applied for unmixing the 2D version of the noisy overlapping MNIST digits. All channels are color scaled to the maximum of the corresponding target channel.

Appendix D: MLE for unmixing 3D-MNIST

Maximum likelihood estimation (MLE) is used as a baseline for the unmixing of 4-channel images with low counts and similar decay constants. The MLE uses the Limited-memory BFGS algorithm [Byrd et al. 1995] from scipy (version 1.10.1). The MLE is used to fit the parameters A_1 , A_2 , A_3 and A_4 in equation 1 over the 3D-MNIST test set. The parameters are bounded between 0 and 1, and normalized to force all abundance parameters to sum to 1 and respect the second axiom of probability. The decay constants are known and fixed. The resulting confusion matrices, obtained over the 800 test images, are shown in Suppl. fig. 4.

$$y(t) = \frac{A_1}{0.1} e^{-t/0.1} + \frac{A_2}{0.2} e^{-t/0.2} + \frac{A_3}{0.3} e^{-t/0.3} + \frac{A_4}{0.4} e^{-t/0.4} \quad (1)$$



Supplementary Figure 4 Channel-wise results on the test set, with ground truth (top), MLE prediction with 4 abundance parameters to adjust (eq. 1, middle) and correlation matrices between true and predicted photons over all pixels from the 3D-MNIST test set (N=800 images, 627,200 pixels).

Appendix E: Acquisition of microscopy images

Sample preparation

Fluorescence microscopy images from both neuronal cell cultures and acute brain slices were included to the datasets used in this study. Primary rat neuronal cell cultures were prepared following established protocols [Nault et al. 2010] in accordance with procedures approved by the animal care committee of Université Laval. Following dissociation from dissected cortex and hippocampus of P0-P1 postnatal rats, cells were plated onto PDL-Laminin coated glass coverslips (12 mm) in a 24-well plate at a density of 100k cells/well. For the β CaMKII dataset, neurons were transfected with a short-hairpin RNA (shRNA) against β CaMKII and/or with the corresponding resistant construct [Nicole et al. 2018], using Lipofectamin 2000. Transfection was done at Days In Vitro (DIV) 8. Cells were fixed for 10 minutes with a 4% PFA solution following an established protocol [Wiesner et al. 2020] at DIV 12 to 15.

Acute mice brain slices were prepared using an optimized version of an established protocol [Bories et al. 2012] in accordance with the procedures approved by the animal care committee of Université Laval. Coronal slices of prefrontal cortex and hippocampus were cut at 400 μ m and kept at 37 degrees Celsius in a slicing solution containing (in mM) 93 NMDG, 20 HEPES, 2.5 KCl, 5 Sodium Ascorbate, 2 Thiourea, 3 Sodium Pyruvate, 0.5 CaCl₂, 10 MgSO₄, 1.2 NaH₂PO₄, 30 NaHCO₃, and 25 glucose, with a pH adjusted between 7.50 - 7.55 and an osmolarity between 300 - 310 mOsm, saturated with 95% O₂ and 5% CO₂ 15 minutes. Slices were transferred at room temperature in Holding Solution containing (in mM) 92 NaCl, 20 HEPES, 2.5 KCl, 1.2 NaH₂PO₄, 25 Glucose, 30 NaHCO₃, 5 Sodium Ascorbate, 2 Thiourea, 3 Sodium Pyruvate, 2 MgSO₄ and 2 CaCl₂, with a pH adjusted between 7.50 - 7.55 and an osmolarity between 300 - 310 mOsm, saturated with 95% O₂ and 5% CO₂. Slices were fixed with 3% glyoxal / 0.8% acetic acid for 24 hours.

After fixation, the cells underwent three 5-minute washes in phosphate-buffered saline (PBS) supplemented with 100 mM glycine. Subsequently, the cells were permeabilized and blocked with a blocking solution composed of 0.1% Triton X-100 and 2% goat serum (GS) in PBS for 30 minutes before proceeding to immunostaining. Immunostaining involved incubation with primary antibodies (PAB) and secondary antibodies (SAB) diluted in the blocking solution at room temperature (RT, Suppl. Table 5). Primary antibodies were allowed to incubate for 2 hours (24 hours for the brain slices), followed by three PBS washes. Secondary antibodies were then applied for 1 hour (2 hours for the brain slices) and subsequently washed three times with PBS. In the case of F-actin labeling, phalloidin fused with STAR635 and diluted in blocking solution, was incubated for 2 additional hours at RT, and subsequently washed three times with PBS. Finally, coverslips were mounted onto slides using Polyvinyl alcohol mounting medium with DABCO (Sigma, cat:10981) and slices were mounted onto slides using mowiol.

Imaging parameters

The FLIM-STED dataset was generated from real 4-channel fluorescence microscopy images acquired with a commercial Abberior Expert Line STED microscope. Three

different combinations of four proteins of interest were labeled with fluorescent dyes that have excitation and emission spectral signatures that allow them to be imaged in different spectral channels on the microscope .

For the first combination, the dendritic marker MAP2 was tagged with ATTO 490LS, the postsynaptic marker PSD95 with STAR635P, the presynaptic marker VGLUT1 with Alexa Fluor 488, and the RNA binding protein Fused in Sarcoma (FUS) with Alexa Fluor 594. PSD95 and FUS were imaged with the STED modality (resolution ~ 50 nm), while MAP2 and VGLUT1 were imaged with the confocal modality (resolution ~ 200 nm).

For the second combination, GFP was used as a cytosolic marker, the tubulin-associated unit (Tau) was labeled with ATTO 490LS, the calcium/calmodulin dependent protein kinase II beta (β CaMKII) with Alexa Fluor 594, and F-actin with Phalloidin STAR635. β CaMKII and F-actin were imaged with the STED modality, while GFP and Tau were imaged with the confocal modality.

For the third combination, the staining was performed in acute brain slices. PSD95 was labeled with a nanobody tagged with Atto643, the vesicular GABA transporter (VGAT) was labeled with Alexa Fluor 594, the presynaptic marker VGLUT1 with Atto490LS, and the scaffolding protein gephyrin with STAR GREEN. VGLUT1, VGAT and PSD95 were imaged with the STED modality, while Gephyrin was imaged with the confocal modality.

The combinations are summarized in Suppl. Table 4 and the antibodies used in Suppl. Table 5.

Further details for the imaging acquisition parameters can be found in Suppl. Table 7. To acquire the real FLIM images, we equipped the microscope with a Time Tagger Ultra 8 from Swabian Instruments GmbH. Experiments were performed in fixed neuronal cultures. The pre-synaptic protein Bassoon was tagged with CF594 and the post-synaptic protein Homer1 was tagged with STAR Orange. These two fluorescent dyes have similar excitation and emission spectra and were imaged using a single imaging channel (605-625 nm) using a 561 nm excitation laser. Further image acquisition details for the FLIM experiments can be found in Table 8.

Number of training images	Number of testing images	Protein 1	Protein 2	Protein 3	Protein 4
10	4	VGLUT1 AF488 Confocal	MAP2 ATTO 490LS Confocal	FUS AF594 STED	PSD95 STAR635P STED
10	4	GFP - Confocal	Tau ATTO 490LS Confocal	β CaMKII AF594 STED	Actin STAR635 STED
10	4	PSD95 STAR635P STED	VGATr AF594 STED	VGLUT1 AF488 STED	Gephyrin STAR GREEN Confocal

Supplementary Table 4 Composition of the 42 intensity images used for building the training and test sets for FLIM-STED.

Primary antibodies			
Antibody	Supplier	Catalogue no.	Dilution
Mouse anti-Bassoon	Enzo	ADI-VAM-PS003	1 : 500
Rabbit anti-Homer1	Synaptic Systems	160003	1 : 500
Mouse anti-MAP2	Sigma-Aldrich	M4403	1 : 1000
Mouse anti- β CaMKII	Invitrogen	13-9800	1 : 100
Rabbit anti-FUS	Sigma-Aldrich	HPA008784	1 : 500
Guinea Pig anti-VGLUT1	Sigma-Aldrich	Ab5905	1 : 500
Guinea-Pig anti-Tau	Synaptic System	314004	1 : 250
Fluotag X2 Anti-PSD95 STAR 635P	Nanotag Biotechnologies	Fluotag X2 Anti-PSD95 635P	1 : 500
Fluotag X2 Anti-PSD95 ATTO643	Nanotag Biotechnologies	N3702-At643-L	1 : 500
Gephyrin	Synaptic Systems	147 021	1 : 500
VGAT	Synaptic Systems	131003	1 : 500
Secondary Antibodies			
Antibody	Company	Catalogue no.	Dilution
GAM CF594	Sigma-Aldrich	SAB4600321	1 : 500
GAR STAR ORANGE	Abberior	STORANGE-1002-500UG	1 : 250
GAM ATTO490LS	Hypermol	2109-1MG	1 : 250
GAGP ATTO490LS	Hypermol	2704-1MG	1 : 250
GAGP Alexa Fluor 488	Sigma-Aldrich	A-11073	1 : 250
GAR Alexa Fluor 594	Invitrogen	A32740	1 : 100
GAM Alexa Fluor 594 Plus	ThermoFisher	A32742	1 : 100
GAM STAR GREEN	Abberior	STGREEN-1001	1 : 250
GAGP ATTO490LS	Hypermol	2704-1MG	1 : 250
(Dye) Phalloidin STAR 635	Sigma Aldrich	30972-20ug	1 : 50

Supplementary Table 5 Antibodies used for immunostaining

Parameter	Confocal	Confocal	STED	STED
	Alexa Fluor 488	Atto 490LS	Alexa Fluor 594	STAR 635P
Excitation wavelength	485 nm	485 nm	561 nm	640 nm
Excitation power	6.6 μ W	6.6 μ W	3.8 μ W	8.4 μ W
Depletion wavelength			775 nm	775 nm
Depletion powers			156 mW	156 mW
Detection wavelengths	500-550 nm	650-720 nm	605-625 nm	650-720 nm
Pixel dwelltime	10 μ s	10 μ s	10 μ s	10 μ s
Line steps	2	2	10	6
Detection gating delay			750 ps	750 ps
Detection gating width			8 ns	8 ns
Pixel size	20 nm	20 nm	20 nm	20 nm
Pinhole size	1.0 A.U.	1.0 A.U.	1.0 A.U.	1.0 A.U.

Supplementary Table 6 Imaging parameters for acquisition of 4-color images (cultures)

Parameter	Confocal Star Green	STED Atto 490LS	STED Alexa Fluor 594	STED Atto 643
Excitation wavelength	485 nm	485 nm	561 nm	640 nm
Excitation power	7.7 μ W	7.7 μ W	3.25 μ W	5.0 μ W
Depletion wavelength		775 nm	775 nm	775 nm
Depletion powers		132 mW	220 mW	132 mW
Detection wavelengths	500-550 nm	650-720 nm	605-625 nm	650-720 nm
Pixel dwelltime	15 μ s	15 μ s	15 μ s	15 μ s
Line steps	6	10	8	4
Detection gating delay		750 ps	750 ps	750 ps
Detection gating width		8 ns	8 ns	8 ns
Pixel size	20 nm	20 nm	20 nm	20 nm
Pinhole size	1.0 A.U.	1.0 A.U.	1.0 A.U.	1.0 A.U.

Supplementary Table 7 Imaging parameters for acquisition of 4-color images (slices)

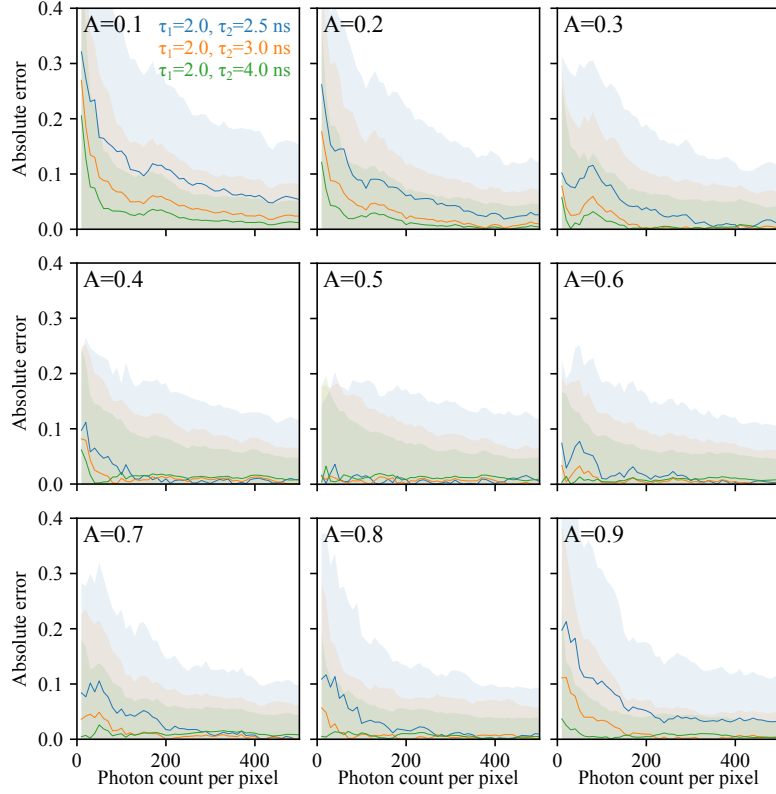
Parameter	Confocal FLIM
Excitation wavelength	561 nm
Excitation power	2.6 μ W
Depletion wavelength	
Depletion powers	
Detection wavelengths	605-625 nm
Pixel dwelltime	15 μ s
Line steps	4
Detection time bins	250 bins of 80 ps range of 20 ns
Pixel size	20 nm
Pinhole size	1.0 A.U.

Supplementary Table 8 Imaging parameters for acquisition of real FLIM images

Appendix F: MLE for FLIM-STED

MLE was tested over pixel counts up to 500 to assess the number of photons required to correctly estimate the relative abundance A , in the case where there are only two components in the pixel and their lifetime values are known (eq. 2). The absolute error between the proportion of the first component (A) predicted by MLE and the actual value is shown in Suppl. fig. 5 for varying numbers of photons, ground truth values of A , and combinations of lifetime values τ_1 and τ_2 . MLE was applied here by bounding the value of A between 0 and 1, and the initial guesses are values between 0 and 1 randomly picked at each iteration. MLE shows lower performance mostly when photon counts are low and the proportion of both classes is unbalanced ($A \neq 0.5$).

$$y(t) = \frac{A}{\tau_1} e^{-t/\tau_1} + \frac{(1-A)}{\tau_2} e^{-t/\tau_2} \quad (2)$$



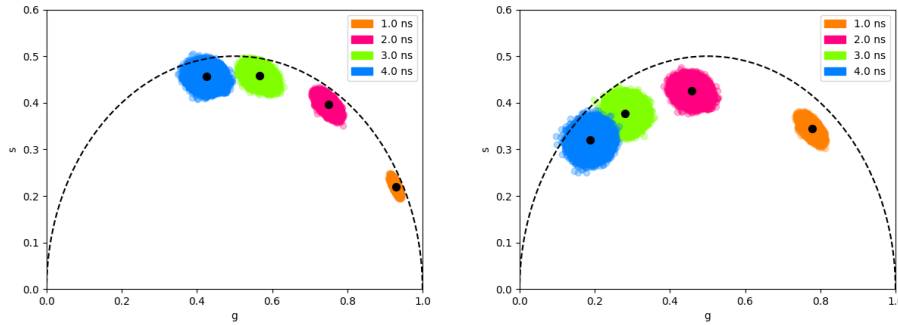
Supplementary Figure 5 Absolute error ($|A_{true} - A_{predicted}|$) between actual and predicted value using MLE for abundance parameter A in eq. 2 for a single simulated pixel. For each graph, target proportion A is incremented by 0.1. Lines show the average of 100 repetitions with different random seeds and initial values, and the shaded region shows the standard deviation.

Appendix G: Phasor analysis method for FLIM-STED

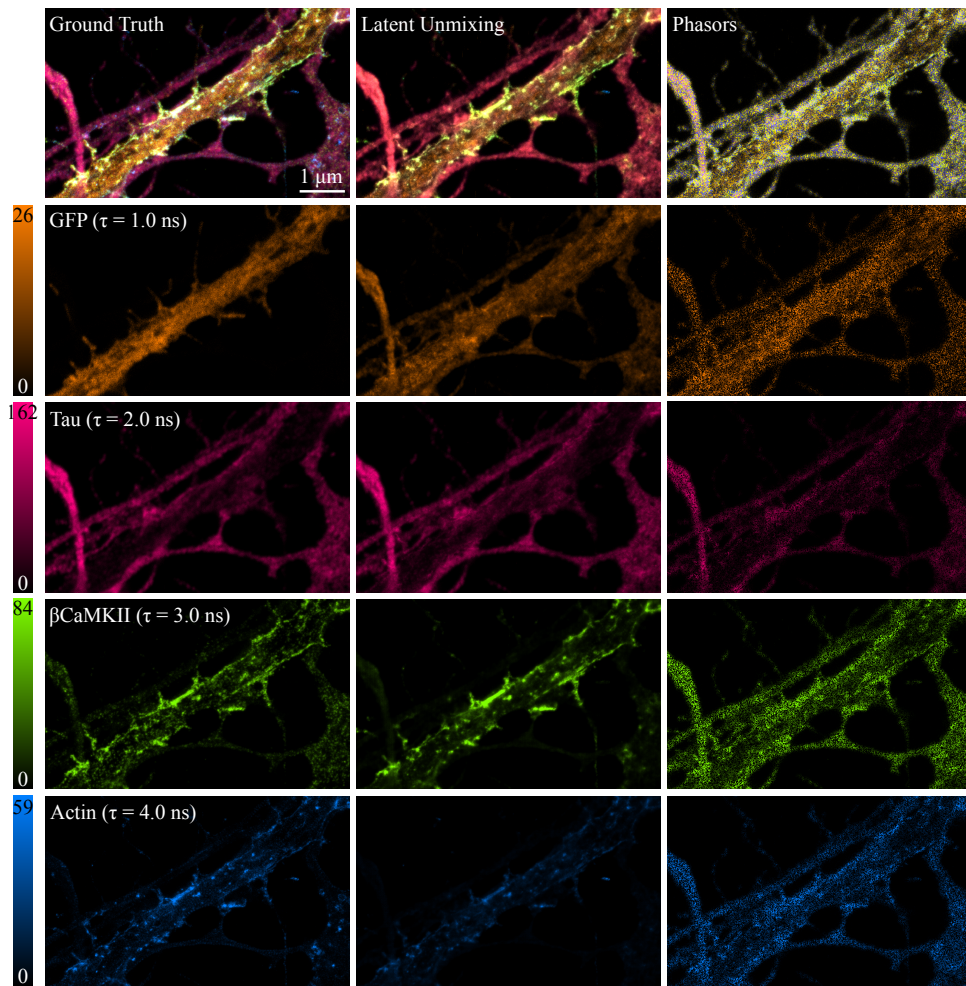
To unmix the FLIM images with the phasor analysis method, we used an established method [Vallmitjana et al. 2022]. We computed the reference positions of each channel using the same control images than for computing the average lifetime for the *Latent Unmixing* method, presented in table 9. For the simulated FLIM test sets, controls were generated from a uniform field of view of 300×300 pixels with 300 photons per pixels, with randomly sampled lifetimes. The proportion of photons assigned to each channel for each pixel is derived from a linear interpolation between the centroid positions of the phasor clusters obtained from the controls (Suppl. fig. 6). We used the first and second harmonics of the Fourier transform to project the decay curves to the phasor space. The raw measurement counts 250 bins of 0.08 ns time delay.

Protein	Dye	# images	Average counts/image	Estimated Lifetime
Homer 1C	STAR Orange	12	1.8×10^5	3.30 ± 0.01 ns
Bassoon	CF 594	12	3.3×10^5	2.40 ± 0.01 ns
Spectrin	CF 594	20	4.2×10^5	2.59 ± 0.05 ns
F-actin	AF 594	20	8.9×10^5	3.29 ± 0.03 ns

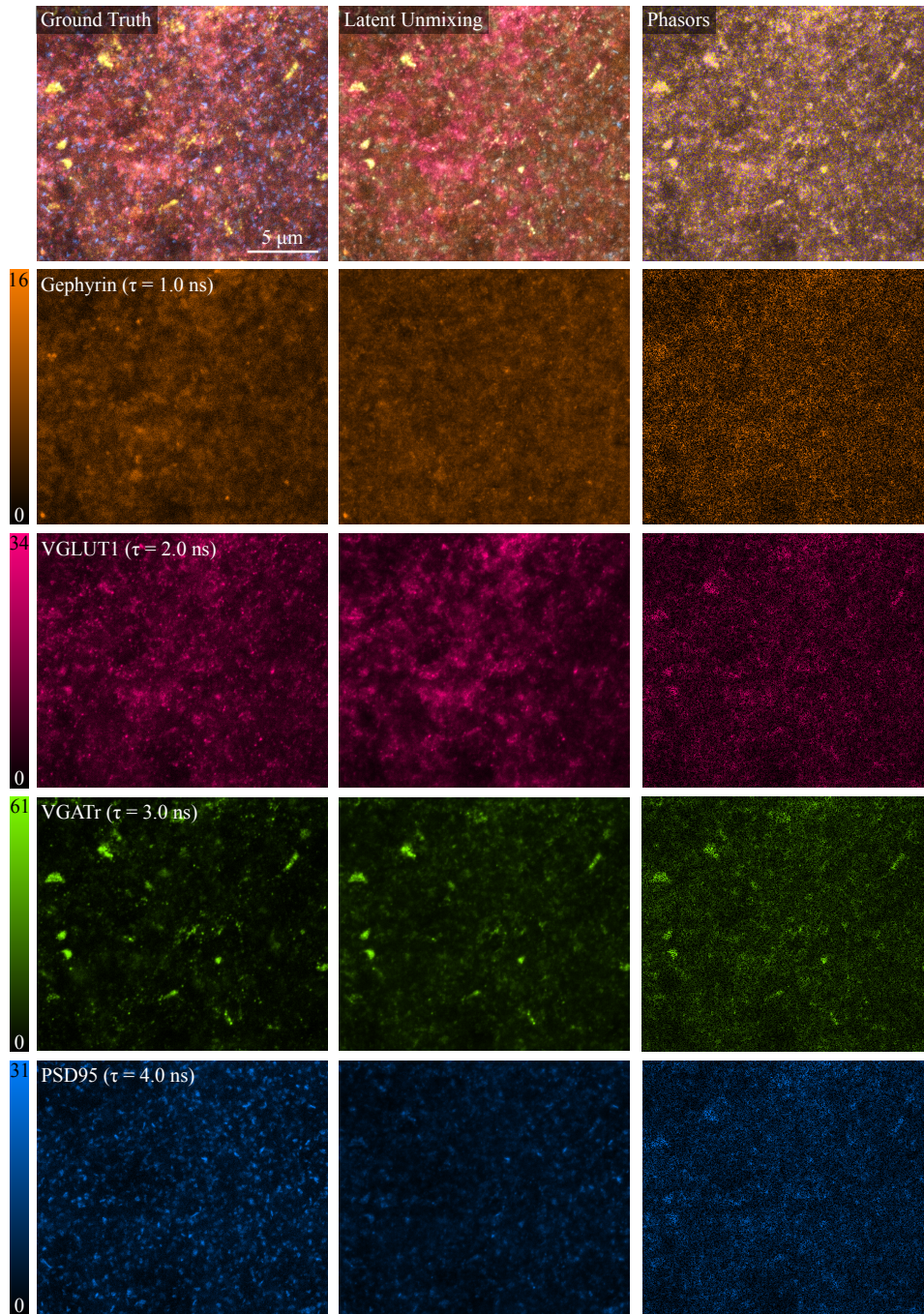
Supplementary Table 9 Lifetime value (mean \pm standard deviation) computed from the maximum likelihood estimation over control samples with a single tagged protein.



Supplementary Figure 6 Phasor plots obtained from simulated controls with 90,000 pixels per channel and 300 photons per pixels. Left and right graphs show first and second harmonics. Each point is a pixel, color-coded by channel. Black points are the centroids of all points belonging to each channel.



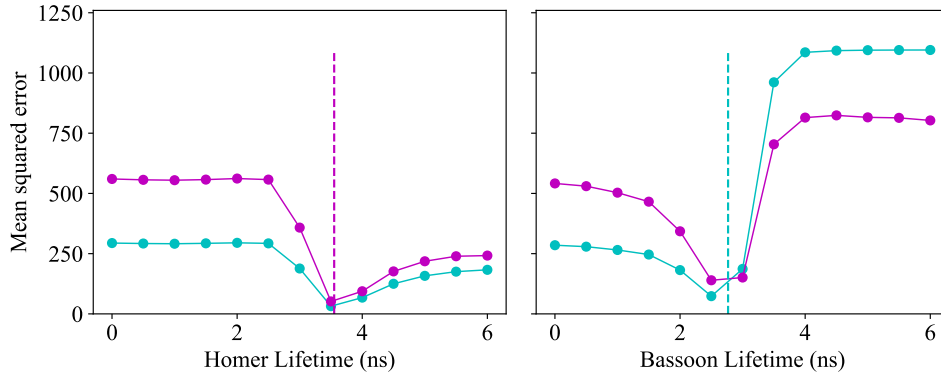
Supplementary Figure 7 Image from the FLIM-STED simulated test set for the unmixing of 4 channels with the *Latent Unmixing* and the phasors analysis methods. All colormaps are scaled from 0 to the 99.9th percentile of the ground truth.



Supplementary Figure 8 Image from the FLIM-STED simulated test set for the unmixing of 4 channels with the *Latent Unmixing* and the phasors analysis methods. All colormaps are scaled from 0 to the 99.9th percentile of the ground truth channels.

Appendix H: Unconditional latent unmixing for FLIM

A version of the *Latent Unmixing* model was trained for two-channels unmixing without conditioning. The lifetime values in training were fixed at 2.77 and 3.55 ns for the Bassoon and Homer channels, respectively. This model could make accurate predictions only if the lifetime values of the test data for both channels was exactly 2.77 and 3.55 ns (Suppl. Fig. 9), rendering the model useless for any biological context where slight deviations in the lifetime are to be expected. This result led us to develop the conditional *Latent Unmixing* model for FLIM data, allowing better generalizability over the lifetime values.



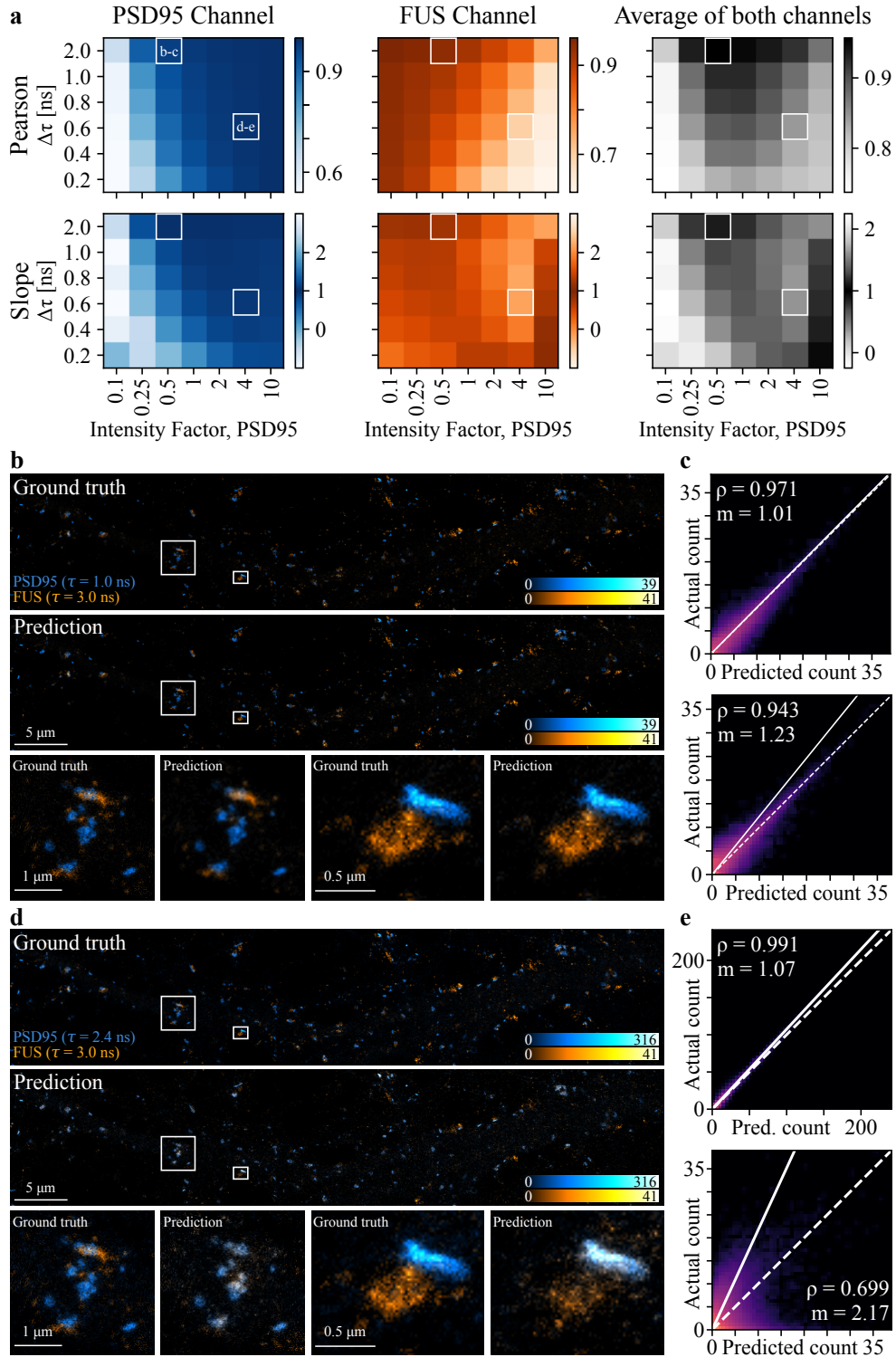
Supplementary Figure 9 Mean squared error between the **unconditional** *Latent Unmixing* prediction and the ground truth for a two-channel image (Bassoon, cyan and Homer, magenta). The performance quickly deteriorates when the lifetime of the test data differs from the lifetime of the training data (2.77 ns for Homer and 3.55 ns for Bassoon, dashed lines).

Appendix I: FLIM-STED Test sets

To test the *Latent Unmixing* method for 4-channel unmixing, a FLIM test set was built from the 12 intensity images with two combinations of lifetime values : $\mathcal{T} = [0.2, 2.1, 4.0, 5.9]$ and $\mathcal{T} = [1.0, 2.0, 3.0, 4.0]$. The first combination was chosen because they are the furthest apart lifetime values that be defined in the $[0, 6]$ ns range. The second combination was chosen as an easy case that could be achieved experimentally, with each lifetime 1 ns apart from the others. We used well separated lifetime values to improve the phasor analysis method’s performance, but even with the most separated values, 4-channel unmixing was still not achievable with this method. This test set counts 24 4-channel images, or 96 single-channel images for computing performance metrics. For 3-channel unmixing, the same 12 intensity images were used to build the test set using the same lifetime combinations ($\mathcal{T} = [0.2, 2.1, 4.0, 5.9]$ and $\mathcal{T} = [1.0, 2.0, 3.0, 4.0]$). We used all possible combinations of 3 channels (and 3 corresponding lifetime values) from the 4 total channels, bringing the total number of 3-channel test images to 96, or 288 single-color channels. For 2-channel unmixing, all combinations of 2 channels (and corresponding lifetime values) were used, resulting in 144 2-channel images, or 288 single-channel images. This is the test set that was used for the qualitative results of figure 5 and the quantitative results of figure 6.

To test the limits in terms of the proximity between lifetime values, a 2-channel test set was generated from the same 12 intensity test images. The lifetime of the second channel is fixed at 3 ns for all generated FLIM images. The lifetime of the first channel was changed from 0.2 ns to 2.8 in increments of 0.2 ns, resulting in 168 2-channel test images or 336 single-channel images for computing the metrics presented in figures 9 and 10.

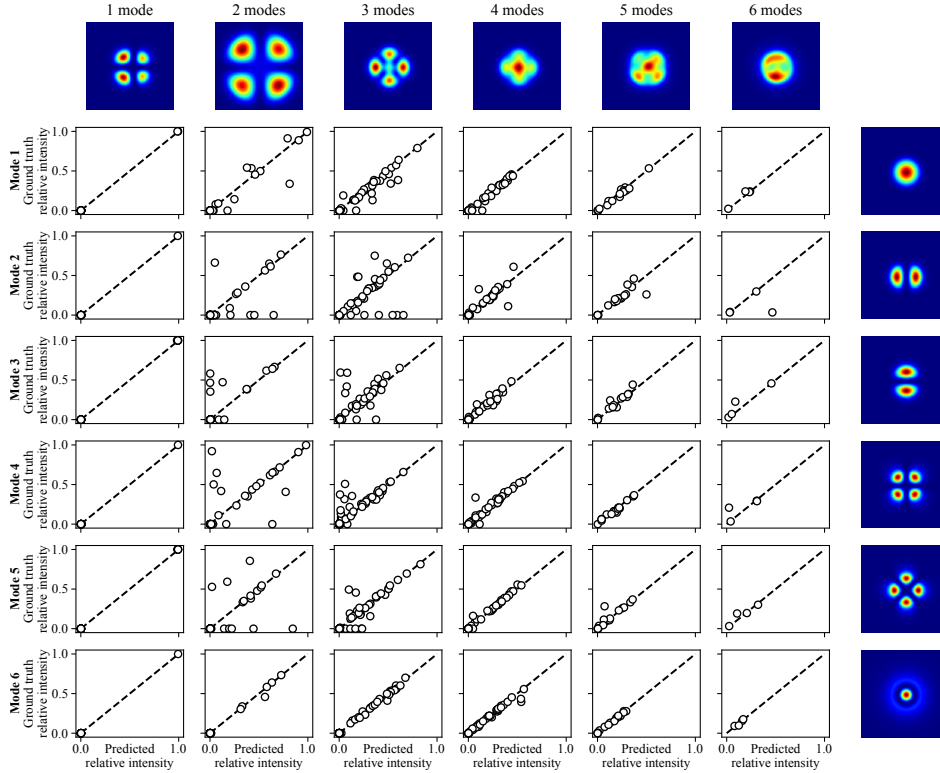
To obtain the results over real FLIM measurements, controls experiment were performed using the integrated FLIM modality in confocal mode. Single-channel images were acquired to measure the average lifetime of the chosen fluorophores. Table 9 shows the lifetime values measured from these controls.



Supplementary Figure 10 Optimization between the signal ratio between two channels and the lifetime proximity. **a**, Pearson correlation coefficient (top) and slope of the linear regression (bottom) between the predicted and actual photon counts for one full field-of-view test image, for different intensity factors of the PSD95 channel and lifetime differences between the two channels. For both metrics, the values closest to 1 (darker colors) are better. **b**, Ground truth and prediction for the full image and for two selected crops, for $\Delta\tau = 2.0$ ns and an intensity factor of 0.5. **c**, Correlation matrices between actual and predicted photon counts for the complete image. **d**, **e**, Same as **b**-**c** for a more difficult case defined by $\Delta\tau = 0.6$ ns and an intensity factor of 4.

Appendix J: Mode decomposition in multi-mode fibers

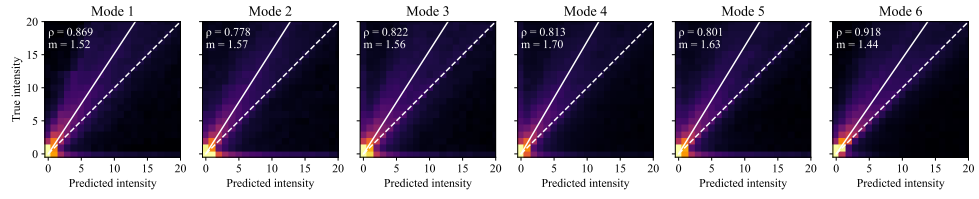
Suppl. Fig. 11 decomposes the data points of Fig. 14 by mode order, also including 0-intensity target modes. Mode decomposition performance does not significantly vary for different spatial distributions, as all modes tend to follow a similar trend towards the diagonal, with a few outliers.



Supplementary Figure 11 Correlation between the target and predicted intensity over different mixtures of propagating modes. Dashed line is the perfect correlation with a slope of 1. Columns correspond to the number of modes in the mixture (from 1 to 6) and rows correspond to a given mode (indexed from 1 to 6). The images in the first row are an example input for each number of modes, summed over the spectral dimension. The images in the last column are an example of the ground truth spatial distribution of each mode.

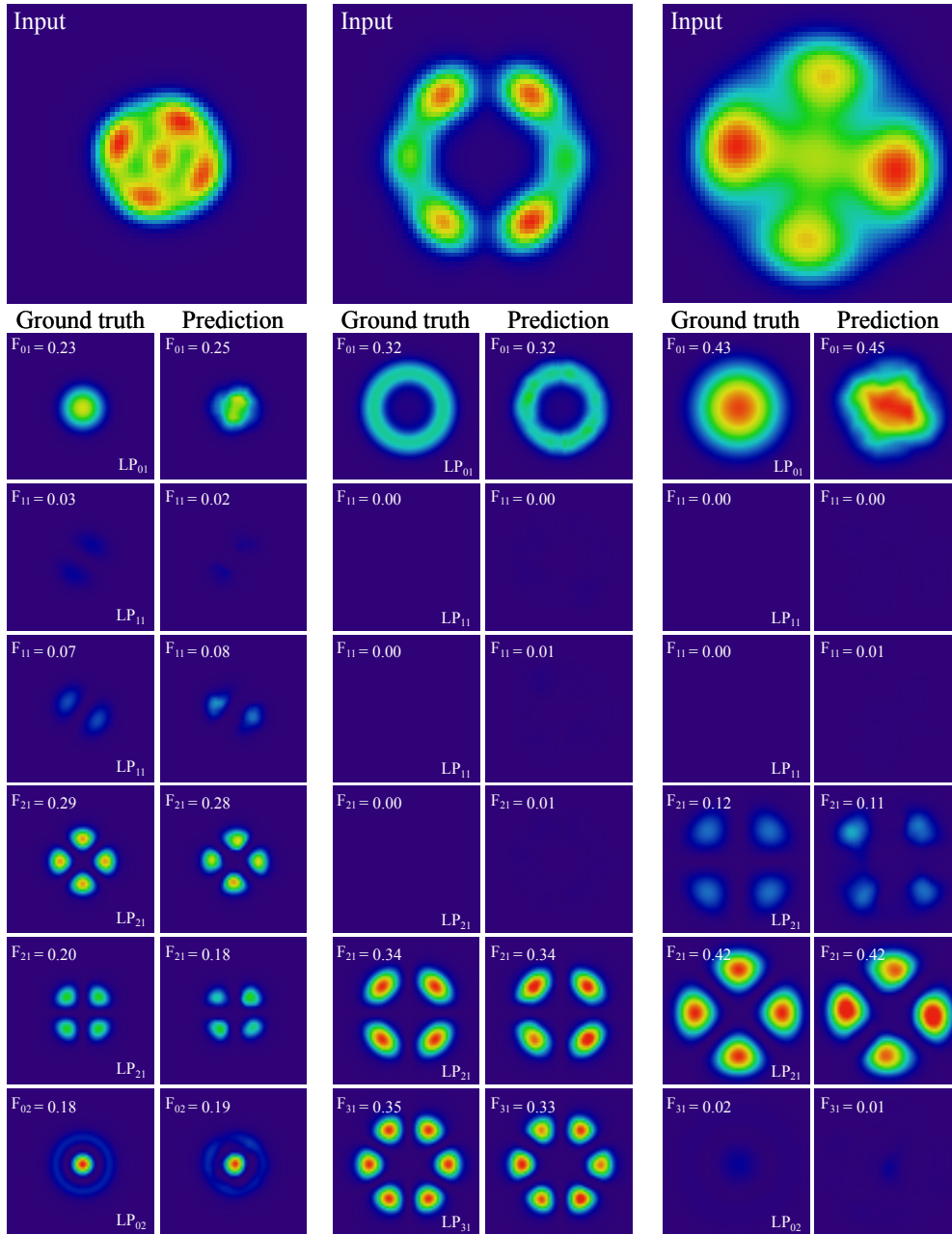
In addition to the correlation between the global relative intensity of each mode, the *Latent Unmixing* method also correctly uncovers their spatial distributions (Suppl. fig. 12). The predicted pixel-wise intensity tends to be under-estimated compared to the ground truth intensity (slope of the regression > 1 , solid white line in Suppl. fig. 12). This is again a result of the model tending to assign some relative intensity to non-propagating modes (non-zero elements where true intensity = 0 in Suppl. fig. 12).

Still, the pixel-wise Pearson correlation coefficient averaged over the whole test set is > 0.77 for all 6 modes.



Supplementary Figure 12 Correlation matrices for each mode of propagation computed over the test set ($N=175$ simulated measurements, 716,800 pixels). Dashed lines correspond to a perfect correlation with a slope of 1. Solid lines show the regression line of the predictions. Pearson correlation coefficients and the slope of the regression between predicted and ground truth are indicated in the top-left corner of each matrix. Colormaps are square-root normalized and scaled to the second maximum of each matrix.

Suppl. fig. 13 shows qualitative results over three different fiber geometries from the test set.



Supplementary Figure 13 Ground truth and predicted spatial distribution of modes for 3 different fiber geometries from three randomly selected examples from the test set. The input as shown is the maximum projection over the spectral dimension of the actual volumetric input. The numbers at the left-upper corner of each image indicates the fraction of the total intensity in each mode. This fraction is obtained by summing the pixels over the image and normalizing over the sum of the 6 images.

Appendix K: Statistical analysis

For statistical analysis, the normality of each distribution is verified with the Shapiro-Wilk test with $\alpha = 0.05$. When both distributions are normal, the null hypothesis that the two groups have the same variance is verified with the F-test with $\alpha = 0.05$. If both variances are equal, the null hypothesis that the two groups have the same average is verified with the T-test for the means of two independent samples. If both variances can not be assumed equal, the same null hypothesis is verified with the Welch's T-test. If at least one of the two distributions is not normal, the null hypothesis is verified with the non-parametric one-way ANOVA test.

For the results presented in figure 9, the null hypothesis of normality could be rejected for all distributions based on the Shapiro-Wilk test. The null hypothesis that the two distributions of samples come from populations with the same median was verified with the non-parametric Mood's median test. For the results presented in figure 10, the null hypothesis of normality could be rejected for all distributions based on the Shapiro-Wilk test. The null hypothesis that the two distributions have the same population mean was verified with the one-way ANOVA test.